Effect of Nano-TiO$_2$ and Polypropylene Fiber on Mechanical Properties and Durability of Recycled Aggregate Concrete

Xiong Wei[1*] , Wang Xiaoqing[1] and Li Chunmei[1]

Abstract

In order to promote the engineering application of recycled concrete, the effects of PPF and nano-TiO2 dioxide on the mechanical properties and durability of recycled concrete were studied.

Polypropylene fiber recycled concrete(PRAC) and nano-TiO2 recycled concrete(TRAC) were prepared by adding different volume contents of PPF and nano-TiO$_2$. The experimental findings demonstrated that the PPF and nano-TiO$_2$ improved the splitting tensile strength of RAC better than the compressive strength. When the volume content of nano-TiO$_2$. and PPF is 0.8% and 1.0%, respectively, the corresponding splitting tensile strength of concrete reaches the maximum value(3.4 and 3.7 MPa). The contribution rates of nano-TiO$_2$ and PPF with different volume contents to the mechanical properties of RAC have optimal values, which are 0.4 and 1.0%, respectively. The incorporation of nano-TiO$_2$ and PPF can effectively inhibit the loss of RAC mass and the generation of pores under freeze–thaw conditions, and slow down the decrease of dynamic elastic modulus. When the volume content of PPF is 1.0% and the volume content of nano-TiO$_2$ is 0.4%, the protection effect on the internal structure of RAC is better, and its carbon resistance is better. The results of RSM model analysis and prediction show that both PPF and nano-TiO$_2$ can be used as admixture materials to improve the mechanical properties and durability of RAC, and the comprehensive improvement effect of PPF on RAC performance is better than that of nano-TiO$_2$.

Keywords Recycled concrete, Polypropylene fiber, Nano-TiO$_2$, Mechanical properties, Concrete durability, RSM analysis model

1 Introduction

With the rapid development of the world economy, various countries have invested more and more in urban construction and infrastructure construction. A large amount of raw materials and concrete have led to the shortage of natural resources such as non-renewable natural aggregates in the short term, and also led to a large amount of construction waste and greenhouse gas emissions, which also has a great negative impact on environmental protection and does not conform to the concept of low-carbon green and sustainable development (Bamigboye et al., 2022; Xu et al., 2022; Qin et al., 2022). Therefore, new materials are urgently needed to replace the consumption of such materials, and recycled aggregate and manufactured sand as alternative materials have gradually become an important branch of the green development of engineering materials in various countries. Recycled aggregate is obtained by reprocessing construction waste, and machine-made sand is obtained by mechanical crushing and screening of industrial waste,

*Correspondence:
Xiong Wei
02009026@whcp.edu.cn
[1] Department of Architecture and Engineering, Wuhan City Polytechnic, Wuhan 430064, China

Wei *et al. Int J Concr Struct Mater*   (2024) 18:28

Page 2 of 22

tailings, and other rocks (Elsayed et al., 2023; Aghajanian et al., 2023; Deng et al., 2023; Alashker & Raza, 2022; Ye et al., 2022; Sun et al., 2022; Li et al., 2021). Şimşek et al. (2022) used recycled coarse aggregate with different substitution amounts (0 ~ 100%) to prepare the mechanical properties of recycled concrete. The results show that the use of coarse recycled concrete aggregate can make the concrete have better compressive strength value with and without the dry–wet cycle and freeze–thaw cycle. Xu Jin et al. (Jin et al., 2022) studied the mechanical properties and erosion depth of recycled aggregate concrete (RAC) with different amounts of high-iron tailings (IOT) in a salt fog erosion environment and erosion process. The results show that IOT makes the compressive strength and splitting tensile strength of RAC increase first and then decrease, and can reduce the porosity of RAC and improve the salt fog erosion resistance. Rui et al. (Yang et al., 2019) studied the effect of manufactured sand on the performance of ultra-high-performance concrete. The results show that the addition of manufactured sand will disturb the particle accumulation skeleton of ultra-high-performance concrete and affect concrete's fluidity and volume stability. Weiguo Shen et al. (Shen et al., 2018) studied the influence of the characteristics of machine-made sand on the performance of machine-made sand concrete. The results show that the particle shape of machine-made sand has little effect on its concrete performance, while the content of stone powder in machine-made sand has performance.

These adverse effects are caused by many pores, many corners, strong water absorption, high crushing index of recycled aggregate and sharp, multi-angle and rough surface of manufactured sand particles. In order to compensate for these adverse effects, scholars have carried out a lot of research on improving the performance of recycled concrete and manufactured sand concrete (Qiuhong et al., 2022; Memon Shazim et al., 2022; Xin et al., 2022; Tao Li et al., 2022; Zhi Liang., 2022; Nattapong et al., 2021; Tam Vivian WY et al., 2020; Hui-lin et al., 2022). Gao Song et al., (2022) analyzed the pore structure parameters and pore size distribution of recycled aggregate concrete by using the mercury intrusion method and fractal dimension theory, and the results show that appropriate admixtures can improve the compressive strength and chloride ion penetration resistance of concrete. Feng C et al., (2022) analyzed the existing biological modification methods, mainly through microbial respiration or enzyme to produce CO_3^{2-}, and to react with Ca^{2+} in soil or concrete to form $CaCO_3$ crystals, to achieve the purpose of filling surface cracks and pores. Wu Jiale et al., (2022) studied the relationship between the shape characteristics of admixture and manufactured sand particles and the properties of concrete. The results show that the shape parameters of manufactured sand particles have a good correlation with the workability and compressive strength of concrete. Shunbo Zhao et al. (Shunbo et al., 2017) studied the effect of machine-made sand on the tensile strength of machine-made sand concrete. The results show that controlling the content of machine-made sand to less than 13% is beneficial to the long-term tensile strength of machine-made sand concrete. With the continuous development of admixture materials, more and more admixture materials are used to improve the performance of recycled concrete and manufactured sand concrete. Among them, various kinds of fiber materials and nano-materials can effectively improve the mechanical properties and durability of concrete such as strength and toughness (Kałuża Marta, 2022; Aleksandrova Olga Vladimirovna et al., 2022; Yang Li et al., 2022; Wisal A, 2023; Hassan A et al., 2023; Shan Haoliang et al., 2022; Yuanxun Zheng et al., 2022). Polypropylene fiber not only has light weight, fine diameter, convenient construction, and low cost but also has good self-dispersion performance and strong chemical corrosion resistance, and it has a very unique role in improving the internal quality of concrete, solving early plastic cracking, and improving the performance of concrete (Wisal & CW. L., 2023). Nano-titanium dioxide (nano-TiO_2), as a photocatalyst, can effectively fill the internal pores of the concrete. It can not only effectively fill the pores of hardened cement paste, but also make up for the initial defects on the surface of recycled aggregate. It also has a unique effect on improving the performance of concrete (Hunar et al., 2022; Twana Ahmed Hussein et al., 2023; Kun et al., 2022; Erfan et al., 2022; Marwan HA et al., 2022).

To better obtain low-carbon green sustainable concrete materials and increase the results in this area, this paper first replaces part of natural coarse aggregate and natural fine aggregate with the composite system of recycled coarse aggregate and manufactured sand to prepare manufactured sand-recycled aggregate concrete. Then, by adding different volume contents (0.8, 1.0, 1.2%) of PPF and different volume contents (0.4, 0.8, 1.2%) of nano-TiO_2, different proportions of PRAC and TRAC were prepared and compared with manufactured sand-recycled aggregate concrete and ordinary concrete, to obtain the influence of PPF and nano-TiO_2 on the mechanical properties of manufactured sand-recycled concrete. Secondly, the effects of PPF and nano-TiO on the durability of manufactured sand-recycled aggregate concrete were analyzed by freeze–thaw cycle test and carbonation test. The design level test of frost resistance and carbonation resistance of manufactured sand-recycled aggregate concrete was carried out by response surface method. The corresponding RSM model was established to analyze the effects of PPF and nano-TiO_2 on the durability of

Wei *et al. Int J Concr Struct Mater*   (2024) 18:28

Page 3 of 22

manufactured sand-recycled aggregate concrete. Finally, the multiple regression equation obtained by the RSM model is used to predict the frost resistance and carbon resistance of the manufactured sand-recycled aggregate concrete. And the error 3D scatter diagram of the real value and the predicted value of the performance of the manufactured sand-recycled aggregate concrete under different freeze–thaw times and carbonation days is obtained. And then the reliability of the analysis model and the advantages and disadvantages of polypropylene fiber and nano-TiO$_2$ are analyzed.

2 Experimental
2.1 Materials
The test cement is P·O42.5 ordinary Portland cement. The aggregates use in the test included a natural fine aggregate, manufactured sand, natural coarse aggregate, and recycled coarse aggregate. The recycled coarse aggregate is the mechanical gravel provided by Wuhan Xintian Transportation Waste Processing Plant, and its source is waste concrete with strength of C30-C50. The fiber use in the test is polypropylene fiber (PPF) with a length of 12 mm. The nano-materials used in the test are nano-TiO$_2$1, and the appearance of each material is shown in Fig. 1.

2.2 Mix Proportion and Specimen Design
The strength grade of the reference concrete prepared in this experiment is C40. The concrete mix ratio is calculated according to the provisions of the specification JGJ55-2011 (2011). The RCA replacement rate is 50%, the length of PPF is 12 mm, the volume content is 0.8,
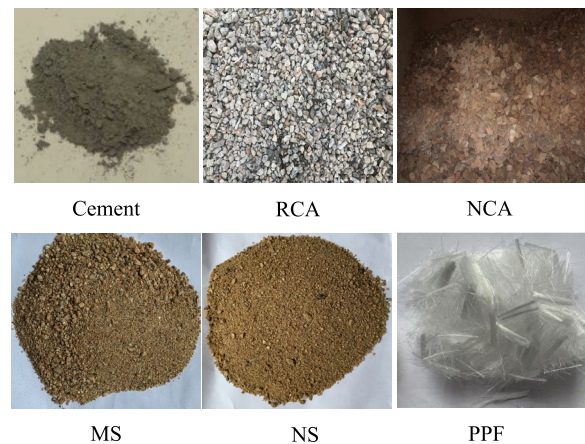

Fig. 1 Material appearance

1.0, and 1.2%, and the nano-TiO$_2$ content is 0.4, 0.8, and 1.2%, respectively. The ordinary concrete and recycled concrete without PPF and nano-TiO$_2$2. The size of the specimen is $100 \times 100 \times 100$ mm cube test block and $100 \times 100 \times 400$ mm prism test block. Before preparing the specimen, PPF and nano-TiO$_2$ should be prepared. When preparing PPF, it is necessary to ensure that the PPF monomer is dispersed and not piled up, to evenly distribute in concrete. When preparing nano-TiO2, it is necessary to add the weighed nano-TiO$_2$ powder into the water, use the DF-101S heat collecting constant temperature heating magnetic stirrer to stir, and then use the 40 kHz ultrasonic wave to disperse continuously for 30 min. The purpose is also to ensure the uniform distribution of TiO$_2$ nano-suspension in concrete. The HJW60

Table 1 Main performance indicators of test materials

Material	Characteristic attribute					
Cement	Density/kg/m^3	Normal consistency/%	Compressive strength/MPa		Splitting tensile strength/MPa	
			7d	28d	7d	28d
	3150	26.6	25.8	44.5	5.6	7.4
NS	Fineness modulus	Apparent density/kg/m3	Bulk density/kg/m3		Mud content/%	
	2.6~2.7	2650	1640		1.8%	
MS	Fineness modulus	Apparent density/kg/m3	Bulk density/kg/m3		Mud content/%	
	2.7	2610	1500		1.5%	
NCA	Grain size/mm	Apparent density/kg/m^3	Bulk density/kg/m^3	water absorption/%	Mud content/%	
	5~30	2660	1350	3.5	0.3	
RCA	Grain size/mm	Apparent density/kg/m^3	Bulk density/kg/m^3	water absorption/%	Mud content/%	
	5~30	2390	1304	6.3	0.3	
PPF	Density/kg/m3	Anti acid alkali	Breaking elongation/%	Elastic modulus/ MPa	Breaking strength/ MPa	
	910	Strong	25±5	>4500	450	
Nano-TiO$_2$	Grain size/mm	Purity/%	Surface area/m^2/g	density/kg/m3	crystal form	
	20	99.9	70–90	3900	R: J=4:1	

Table 2 Mix proportion design of RAC

No	PPF/%	Nano-TiO$_2$/%	Material consumption (kg/m^3)						
			Cement	NS	MS	NCA	RCA	Water	Water reducer
NAC	0	0	450	535	134	1092	0	180	3.65~4.71
RAC	0	0	450	535	134	546	546	180	3.65~4.71
P$_{V0.8}$RAC	0.8	0	450	535	134	546	546	180	3.65~4.71
P$_{V1.0}$RAC	1.0	0	450	535	134	546	546	180	3.65~4.71
P$_{V1.2}$RAC	1.2	0	450	535	134	546	546	180	3.65~4.71
T$_{V0.4}$RAC	0	0.4	450	535	134	546	546	180	3.65~4.71
T$_{V0.8}$RAC	0	0.8	450	535	134	546	546	180	3.65~4.71
T$_{V1.2}$RAC	0	1.2	450	535	134	546	546	180	3.65~4.71

single horizontal shaft concrete mixer was used in the test. Firstly, coarse aggregate, fine aggregate and cement are added and stir for 60 s. After stirring evenly, the poly-acid superplasticizer and water are evenly stirred and poured into the mixer for continuous stirring for 90 s. The fluidity of the mixture in the mixer is observed, and then the recycled concrete with PPF and the recycled concrete with nano-TiO$_2$ are prepared in batches. When adding PPF and nano-TiO$_2$, it is necessary to uniformly and slowly add them to the concrete under the premise of the operation of the mixer and appropriately extend the concrete mixing time to make PPF and nano-TiO$_2$ evenly dispersed in the concrete matrix. Finally, the fresh concrete is poured into the molds of 100×100×100 mm and 100×100×400 mm with the demolding agent, and the test piece is formed by using the shaking table to vibrate and compact. After standing at room temperature for 24 h, the mold is molded, and the mechanical properties and durability tests are carried out after 28 days of standard curing.

2.3 Experimental Design

2.3.1 Basic Mechanics Test

According to the provisions of the standard GB/T 50081–2019 (2019), this paper uses the DYE-2000S micro-computer servo pressure tester produced by Cangzhou Zhulong Engineering Instrument Co., Ltd. to carry out the compressive test and splitting tensile test on specimens with a size of 100×100×100 mm. In the compression test, two pairs of flat opposite surfaces are selected as the bearing surface, and the center of the specimen is placed in the center of the tray. In the splitting tensile test, the specimen is placed between two stainless steel semi-cylindrical pads, and a wooden pad is pasted on the contact between the pad and the specimen to ensure that the center line of the test block, the center line of the pad and the center of the pad are aligned, as shown in Figs. 2, 3. Then the parameters of the test machine are set, the
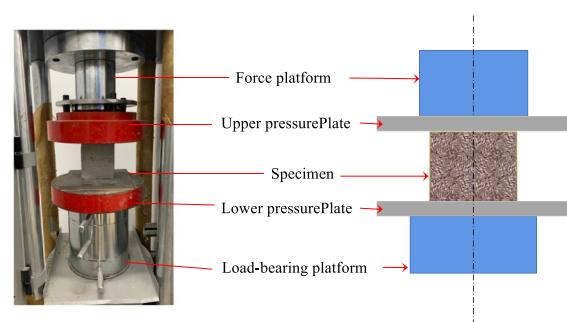
**Fig. 2** Specimen compressive test diagram
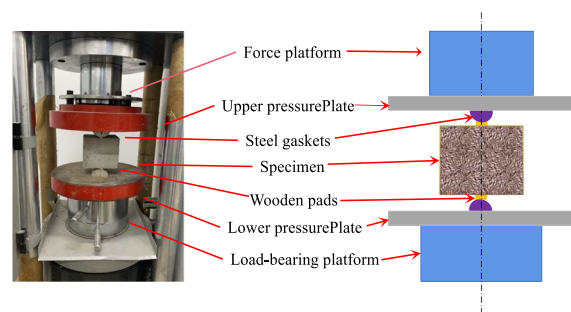
Fig. 3 Specimen splitting tensile test diagram

loading speed is set to 0.5 MPa/s, and the instrument is calibrated. Finally, the test process is observed and the photo record is taken. After the specimen is unstable and destroyed, the loading is automatically stopped and the value displayed on the display screen is read.

2.3.2 Freeze–Thaw Cycle Test

According to the provisions of the standard GB/T50082-2009 (2009), and the use of Hebei Tianjian Engineering Instrument Co., Ltd. TDR-I III type concrete rapid freeze–thaw test machine for the freeze–thaw test of specimens, as shown in Fig. 4. When the freeze–thaw
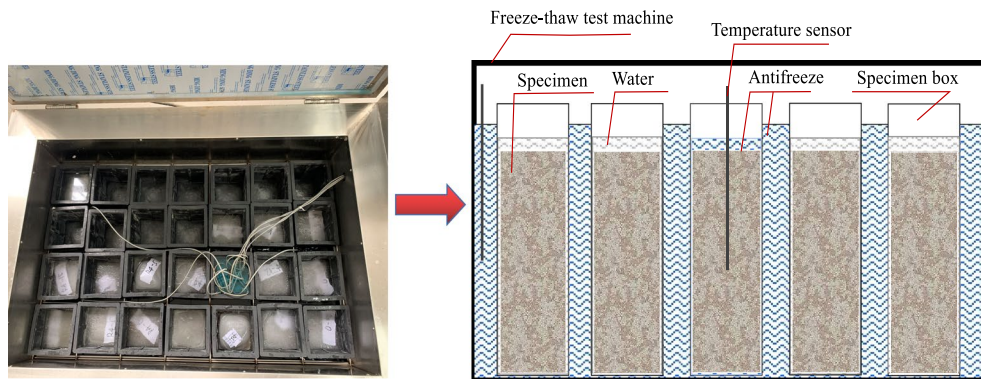
Fig. 4 Freeze–thaw cycle test diagram

cycle is carried out, the specimen cured for 28 days needs to be taken out from the standard curing room, after the appearance inspection, it is immersed in water at 15 ~ 20 ℃ for 4 h, then the specimen is taken out, the surface water is wiped off with a wet cloth, and the weight and dynamic elastic modulus are measured. Secondly, the specimen is placed in the specimen box, and tap water is injected to ensure that the liquid level is 5 mm higher than the top surface of the specimen. Finally, the specimen box is placed in the freeze–thaw instrument, and the specimen box containing the temperature measuring specimen is placed in the middle position of the freeze–thaw instrument, and then the instrument is opened for the freeze–thaw cycle.

2.3.3 Anti-Carbonization Test

According to the provisions of the specification GB/T50082-2009 (2009), the TH-B concrete carbonation testing machine of Shanghai Meiyu Co., Ltd. was used to carry out the carbonation test on the specimens, as shown in Fig. 5. During the carbonization test, the specimens that were cured for 26 days were taken out from the standard curing room, and the specimens were dried at 60℃ using a programmable constant temperature and humidity test chamber. After 48 h, the specimens were taken out, and the remaining surfaces of the two opposite sides were sealed with paraffin. A parallel line was drawn every 10 mm in the direction of the extension on the side to determine the position of each measuring point. Then,
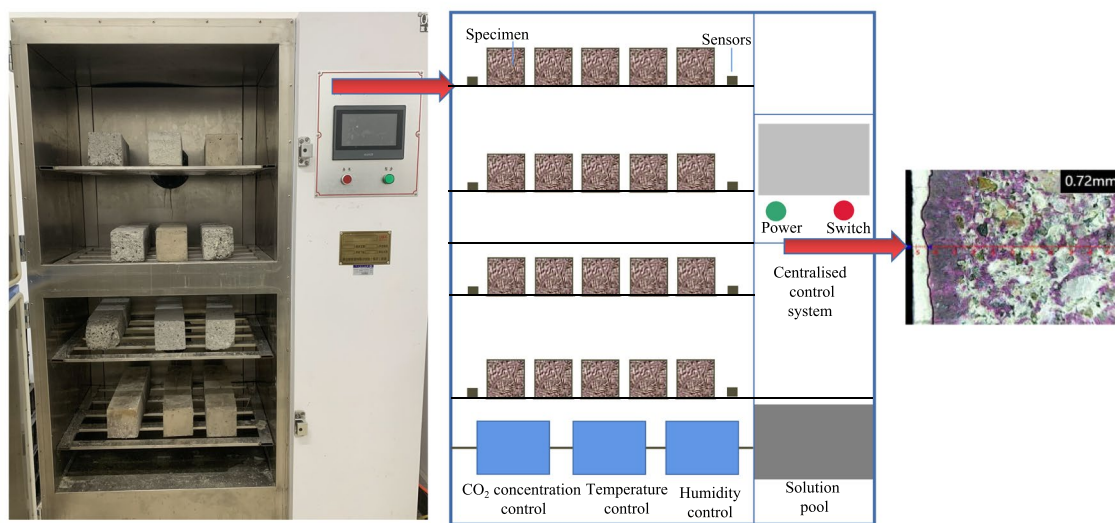
Fig. 5 Carbonization test diagram

Wei *et al. Int J Concr Struct Mater*   (2024) 18:28

Page 6 of 22

the specimens of each group were placed in the carbonization test box for carbonization test, and the carbonization ages were 3, 7, 14, and 28 days, respectively, to ensure that the two sides of the specimen can be fully exposed to CO_2, the spacing of the test blocks in the carbonization box should be guaranteed above 50 mm. Finally, the specimens of the corresponding age were taken out and broken from one end of the specimen on the press. The thickness of each removal was 50 mm, and the rest was put into the carbonization test box again with a paraffin cover to continue carbonization. At the same time, the residual powder on the section was removed, and then 1% phenolphthalein alcohol solution was dropped. After 30 s, the carbonation depth was measured at the previously determined measuring point using an electronic vernier caliper.

2.4 Conclusion and Analysis
2.4.1 Results and Analysis of Mechanical Test

According to different nano-TiO_2 and PPF volume content, 7 groups of RAC specimens with different proportions are set up. The compressive strength and splitting tensile strength tests of RAC with different proportions under different freeze–thaw cycles are carried out. The strength of the corresponding specimen is calculated by using the load at the time of failure of the specimen by (1) and (2). The results are shown in Figs. 6, 7. According to the provisions of the standard GB50204-2002 (2011), when the specimen is a cube test block with a side length of 100 mm or the maximum particle size of the aggregate ≤ 31.5 mm, the standard value of the compressive strength of the concrete cube should be multiplied by the strength size conversion coefficient 0.95, and the standard value of the splitting tensile strength should be multiplied by the strength size conversion coefficient 0.85:
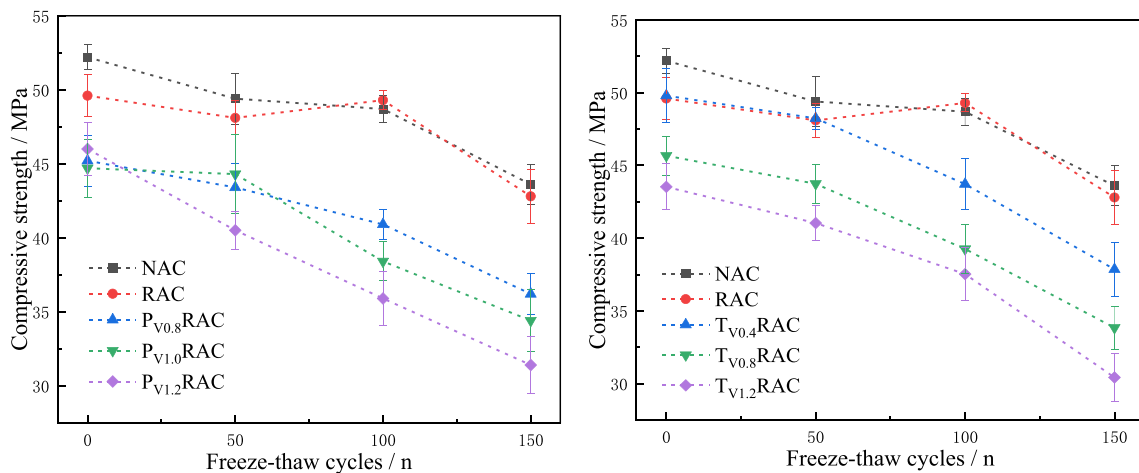

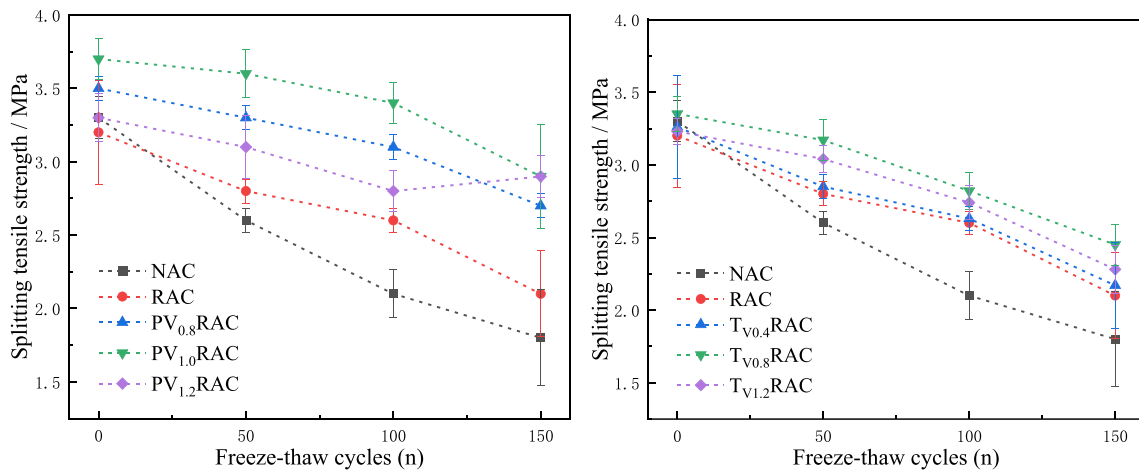
Fig. 6 Variation trend diagram of compressive strength

Fig. 7 Variation trend diagram of splitting tensile strength

$$f_{cu} = 0.95 \frac{F}{A} \tag{1}$$

$$f_{ts} = 0.85 \frac{2F}{\pi A} \tag{2}$$

In the formula:

f_{cu}, f_{ts}, f_t: the compressive strength, splitting tensile strength and flexural strength of concrete specimens, respectively, and the unit is MPa; F: ultimate load on concrete specimens and the unit is kN; A—the compression area of the concrete specimen during the test, and the unit is mm^2.

From Figs. 6, 7, when the specimen is not freeze-thawed, the compressive strength of all the specimens exceeds the C40 standard value, and the compressive strength and splitting tensile strength of NAC are higher than those of the control and RAC, indicating that the addition of recycled coarse aggregate leads to the deterioration of the workability of recycled concrete, which makes the hydration reaction inside the concrete insufficient and reduces the strength. The compressive strength of the specimens mixed with nano-TiO$_2$ is higher than that of the specimens mixed with PPF, and the splitting tensile strength is the opposite. The compressive strength and splitting tensile strength of the specimens with PPF are up to 46 and 3.7 MPa, respectively, which are increased by − 7.26 and 15.63%, respectively, compared with RAC. The compressive strength and splitting tensile strength of the specimens with nano-TiO$_2$ are up to 49.8 and 3.4 MPa, respectively, which are increased by 0.4 and 6.25%, respectively, compared with RAC, indicating that nano-TiO$_2$ can effectively compensate for the defects of recycled coarse aggregate. However, its effect on the ductility of concrete is lower than that of PPF. With the increase in freeze–thaw cycles, the compressive strength and splitting tensile strength of the specimens with different proportions decrease, and the strength of the test group and the control group (NAC and RAC) have obvious stratification, especially the compressive strength of the specimens, indicating that nano-TiO$_2$ and PPF had more obvious effects on the compressive strength of the specimens. With the increase of freeze–thaw times, when the content of nano-TiO$_2$ and PPF is 0.4 and 0.8%, respectively, the compressive strength damage of the specimen is relatively the lowest, and when the content of nano-TiO$_2$ and PPF is 0.8% and 1.0%, respectively, the splitting tensile strength damage of the specimen is relatively the lowest, indicating that under freeze–thaw conditions, the compressive strength improvement effect of nano-TiO$_2$ and PPF on the specimen decreases with the increase of volume content, and the splitting tensile strength improvement effect of the specimen increases first and then decreases with the increase of volume content. From Fig. 7, it can be concluded that the trend of splitting tensile strength of specimens with PPF content is evenly dispersed, while the trend of splitting tensile strength of specimens with nano-TiO$_2$ content is relatively concentrated, indicating that under freeze–thaw conditions, the effect of PPF on splitting tensile strength of concrete is better than that of nano-TiO$_2$.

2.4.2 Contribution of Nano-TiO2 and PPF to Mechanical Properties of RAC

In this part, the number of freeze–thaw cycles is used as a variable, and the contribution rate Q of the volume content of nano-TiO$_2$ and PPF is used as a dependent variable (Yanru et al., 2020) to explore the effect of nano-TiO$_2$ and PPF on the compressive strength and splitting tensile strength of RAC after freeze–thaw. The greater the contribution rate, the more obvious the nano-TiO$_2$ and PPF slow down the loss of compressive and splitting tensile strength after RAC freeze–thaw, and the better the frost resistance of RAC. The calculation formula is as follows (3), (4):

$$Q_{c,V} = \frac{f_{cV,N}}{f_{cV,0}}, \tag{3}$$

$$Q_{t,V} = \frac{f_{tV,N}}{f_{tV,0}}. \tag{4}$$
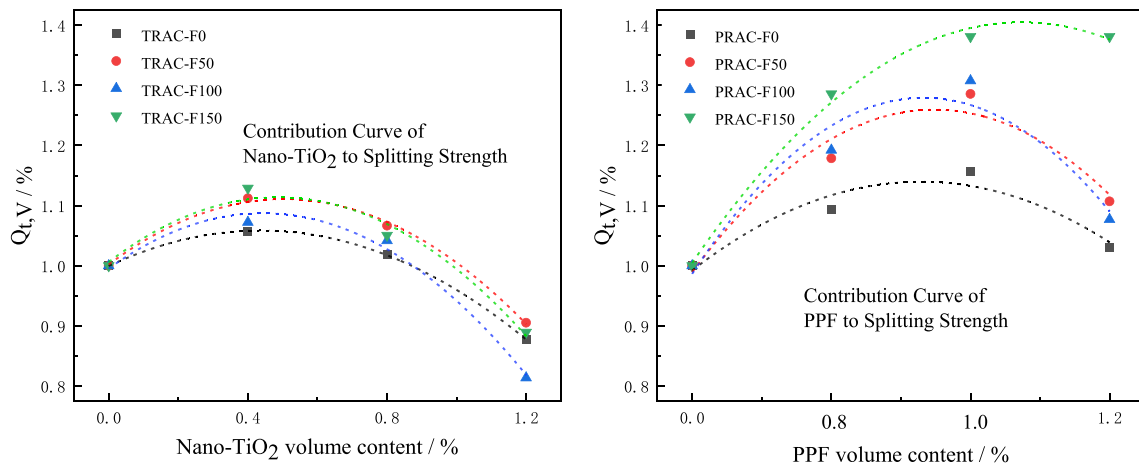
In the formula:

$Q_{c,V}$ and $Q_{t,V}$: when the volume content of nano-TiO$_2$ and PPF is V, the contribution rate of nano-TiO$_2$ and PPF to compressive strength and splitting tensile strength, respectively; $f_{V,N}$: when the volume content is V, the strength of RAC after N freeze–thaw cycles; $f_{V,0}$: when the volume content is V, the strength of RAC without freeze–thaw cycles.

Through (3) and (4), the relationship between the volume content of different nano-TiO$_2$ and PPF and their contribution to compressive strength and splitting tensile strength after 0,50,100,150 freeze–thaw cycles (*F0, F50, F100, F150*) was fitted, respectively, as shown in Figs. 8, 9. Tables 3, 4 are the fitting curves of the contribution rate corresponding to different nano-TiO2 and PPF volume contents under freeze–thaw cycle conditions.

From Figs. 8, 9, the contribution value of different nano-TiO$_2$ and PPF content to the compressive strength of RAC specimens decreases with the increase of content, and the contribution value to the splitting tensile strength of RAC specimens increases first and then decreases with the increase of content. From the contribution rate of nano-TiO$_2$ and PPF to the tensile

Wei *et al. Int J Concr Struct Mater*   (2024) 18:28

Page 8 of 22
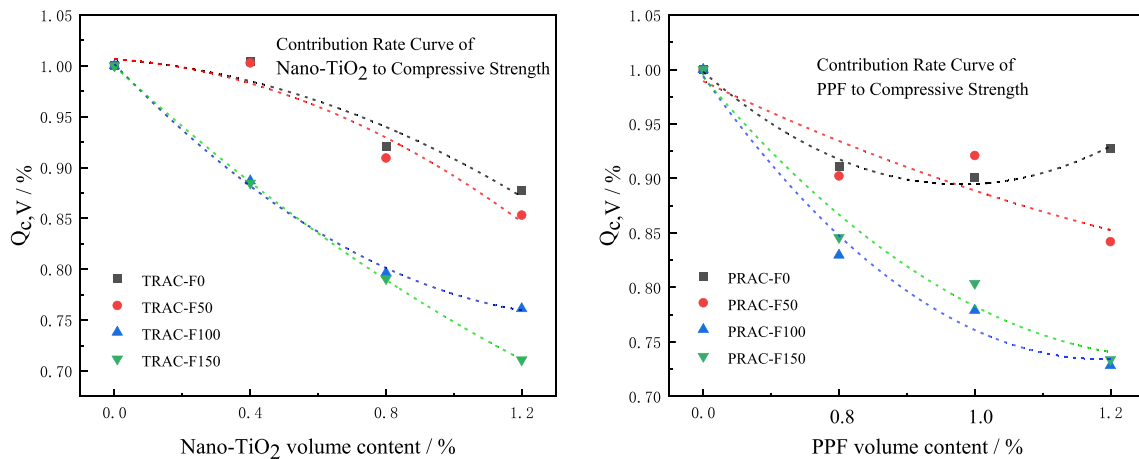
Fig. 8 Contribution curves of nano-TiO2 and PPF to compressive strength

Fig. 9 Contribution curves of nano-TiO$_2$ and PPF to splitting tensile strength

Table 3 The fitting function of the contribution rate of nano-TiO2 and PPF volume content to compressive strength

Cycle index/n	PPF content (0、0.8%、1.0%、1.2%)	Nano-TiO2 content (0、0.4%、0.8% 、1.2%)
0	$y = 0.1796 \times 2 - 0.2724x + 0.9979$ $R^2 = 0.985$	$y = -0.0737 \times 2 - 0.0241x + 1.0064$ $R^2 = 0.9295$
50	$y = 0.0292 \times 2 - 0.1489x + 0.9893$ $R^2 = 0.8201$	$y = -0.0923 \times 2 - 0.0228x + 1.0067$ $R^2 = 0.9441$
100	$y = 0.187 \times 2 - 0.4409x + 0.994$ $R^2 = 0.9829$	$y = 0.122 \times 2 - 0.3481x + 1.0016$ $R^2 = 0.9984$
150	$y = 0.1314 \times 2 - 0.368x + 0.993$ $R^2 = 0.9742$	$y = 0.0557 \times 2 - 0.3072x + 0.9996$ $R^2 = 0.9999$

strength in Fig. 8, the contribution value of nano-TiO$_2$ and PPF to the compressive strength of the test group decreased significantly with the increase of the number of freeze–thaw cycles. This is because the recycled coarse aggregate has a rough surface and many

edges and corners, which will accelerate the shedding of the aggregate after a certain number of freeze–thaw cycles, resulting in a decrease in the contribution value of nano-TiO$_2$ and PPF to the compressive strength of the test group. When the freeze–thaw cycle is 100, the

Wei *et al. Int J Concr Struct Mater*   (2024) 18:28

Page 9 of 22

Table 4 The fitting function of the contribution rate of nano-TiO2 and PPF volume content to splitting tensile strength

Cycle index/n	PPF content (0、0.8%、1.0%、1.2%)	Nano-TiO2 content (0、0.4%、0.8%、1.2%)
0	$y = -0.3418 \times 2 + 0.4492x + 0.9922$ $R^2 = 0.9153$	$y = -0.3105 \times 2 + 0.2709x + 0.9995$ $R^2 = 0.9998$
50	$y = -0.558 \times 2 + 0.7768x + 0.9893$ $R^2 = 0.9471$	$y = -0.4276 \times 2 + 0.4307x + 1.0021$ $R^2 = 0.9963$
100	$y = -0.6611 \times 2 + 0.8798x + 0.9865$ $R^2 = 0.9333$	$y = -0.4693 \times 2 + 0.4159x + 0.9952$ $R^2 = 0.9888$
150	$y = -0.4464 \times 2 + 0.8452x + 1.0048$ $R^2 = 0.9953$	$y = -0.4536 \times 2 + 0.4418x + 1.0062$ $R^2 = 0.9744$

contribution rate is greatly reduced, and this is because nano-TiO$_2$ and PPF are constrained in the concrete, but nano-TiO$_2$ particles have a certain improvement effect on the compactness of the concrete, which can effectively reduce the freeze–thaw damage of the compressive strength of the concrete. The increase in PPF content leads to a larger contact area with recycled aggregate. With the increase in freeze–thaw times, the damage to the compressive strength of specimens is further accelerated. The results show that the contribution of nano-TiO$_2$ to the compressive strength of the specimen is higher than that of PPF under freeze–thaw conditions. From Fig. 9, no matter how many freeze–thaw cycles, the contribution rate of nano-TiO$_2$ and PPF to the splitting tensile strength of the specimen increases first and then decreases with the increase of the content, and the contribution rate of PPF to the splitting tensile strength of the specimen is higher than that of nano-TiO$_2$, indicating that PPF is more conducive to the improvement of the splitting tensile strength of the specimen under freeze–thaw cycles. From Tables 3, 4 except that the R2 of the specimens with PPF is less than 0.9 when the number of freeze–thaw cycles is 50, the fitting functions of the other contribution rates are higher than 0.9, indicating that

the reliability of the fitting functions of each contribution rate is good. From the fitting function, the optimal content of nano-TiO$_2$ and PPF corresponding to the optimal contribution rate of the mechanical properties of the specimens can be obtained, which are 0.4% and 1.0%, respectively.
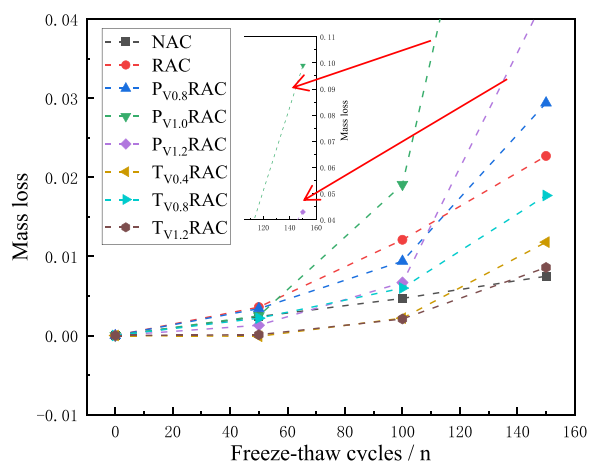
2.4.3 Mass Changes of Specimens Under Different Freeze–Thaw Cycles

After different freeze–thaw cycles, the surface of the prism block of $100 \times 100 \times 400$ mm will be damaged and fall off due to the freeze–thaw cycle, resulting in the loss of the quality of the specimen and the reduction of the performance. Table 5 is the quality change of the specimen after different freeze–thaw times.

Table 5 shows that the mass loss rate of each specimen shows an overall upward trend with the freeze–thaw cycle. However, due to the initial cracks and holes in the recycled concrete itself, the water absorption rate in the early stage of freeze–thaw increases, and the mortar on the outer surface of the specimen does not fall off obviously. Therefore, when the freeze–thaw cycle is 50 times, the mass of the specimen is not significantly reduced, and the reduction is less than 0.4%. However, when the freeze–thaw cycle is 150 times, the mass loss of the test

Table 5 Mass of specimens under different cycles

No	Mass changes of specimens under different cycles/kg							
	0 times	Change ratio	50 times	Change ratio	100 times	Change ratio	150 times	Change ratio
NAC	9.2295	0	9.2070	0.0024	9.1865	0.0047	9.1602	0.0075
RAC	9.399	0	9.3655	0.0036	9.2855	0.0121	9.1855	0.0227
P$_{V0.8}$RAC	9.376	0	9.344	0.0034	9.288	0.0094	9.1	0.0294
P$_{V1.0}$RAC	9.412	0	9.388	0.0025	9.232	0.0191	8.48	0.0990
P$_{V1.2}$RAC	9.588	0	9.576	0.0013	9.524	0.0067	9.176	0.0430
T$_{V0.4}$RAC	9.2025	0	9.2035	−0.0001	9.182	0.0022	9.094	0.0118
T$_{V0.8}$RAC	9.472	0	9.4515	0.0022	9.415	0.0060	9.3045	0.0177
T$_{V1.2}$RAC	9.3645	0	9.3635	0.0001	9.345	0.0021	9.284	0.0086

Wei *et al. Int J Concr Struct Mater*   (2024) 18:28

Page 10 of 22

Fig. 10 Mass loss of specimens under different freeze–thaw cycles

group is more than 1%. The mass loss diagram shown in Fig. 10 is obtained from Table 5. From Fig. 10, when nano-TiO_2 and PPF are not incorporated, the mass loss of NAC in different freeze–thaw cycles is less than that of RAC. When the number of freeze–thaw cycles is 150, the mass loss of NAC is 0.75%, while the mass loss of RAC reaches 2.27%, which is 3 times that of NAC, indicating that the incorporation of recycled aggregate will greatly weaken the frost resistance of concrete specimens. The effects of nano-TiO_2 and PPF on the frost resistance of RAC are similar when the number of freeze–thaw cycles did not exceed 100 times. When the number of freeze–thaw cycles exceeds 100 times, the mass loss curve of

RAC mixed with PPF is in the upper part. When the volume content of PPF is 1.0%, the mass loss rate reaches the maximum (9.9%). The maximum mass loss of RAC doped with nano-TiO_2 is less than 2%, and the mass loss of RAC doped with nano-TiO_2 is lower than that of RAC without nano-TiO_2. When the volume fraction of nano-TiO_2 is 1.2%, the mass loss curve of RAC is below the NAC mass loss curve, indicating that when the number of freeze–thaw cycles exceeds 100 times, PPF is not conducive to the improvement of RAC frost resistance, which will lead to the increase of RAC mass loss, while nano-TiO_2 incorporation can effectively reduce the mass loss of RAC. When the volume content of nano-TiO_2 is 0.4 and 1.2%, the frost resistance of RAC is better. When the freeze–thaw cycle is 150 times and the volume content of nano-TiO_2 is 1.2%, the mass loss of RAC is the lowest (0.86%), and the frost resistance is the best. This is because nano-TiO_2 has the characteristics of small particle size, high specific area and good stability, which can well fill the micro-pores inside the concrete, so that the concrete has good environmental adaptability.

2.4.4 Internal Porosity of RAC Under Freeze–Thaw Cycles

After 150 freeze–thaw cycles, the specimens with different volume contents of nano-TiO_2 and PPF were cut by cutting machine, and the pores of the section were filled with white wall repair paste. Then, the pores of the recycled concrete section before and after the freeze–thaw cycle were processed by image gray scale, the gray scale image was binarized and the pore ratio
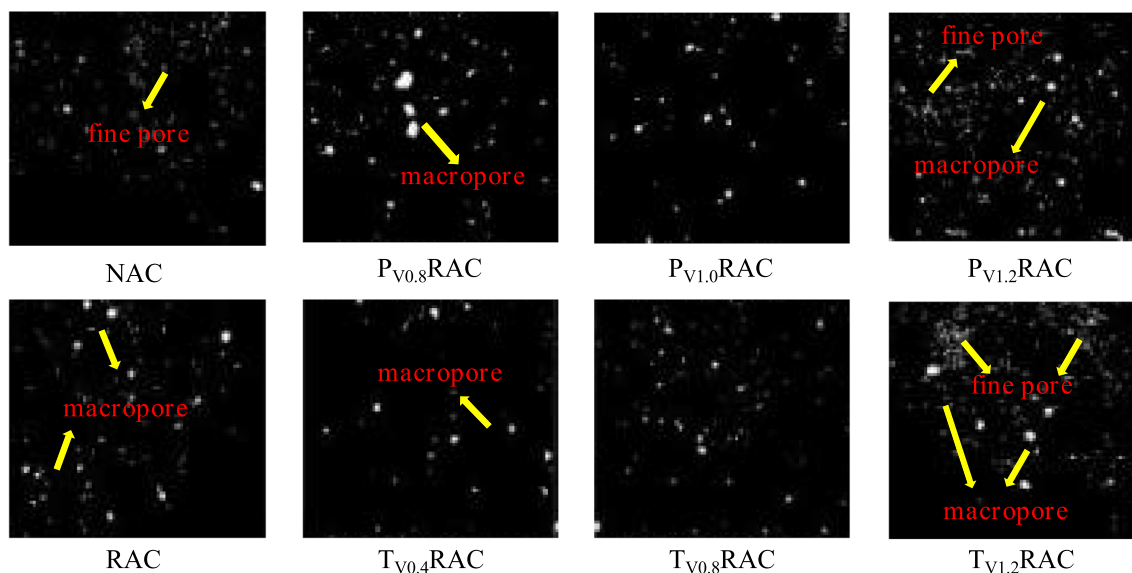
Fig. 11 Sectional pore diagram of RAC with different volume fractions of nano-TiO2 and PPF

was identified. The output results are shown in Fig. 11. From Fig. 11 that after 150 freeze–thaw cycles, the white part of the specimen section accounts for a large proportion. The NAC section of the control group is dominated by fine pores, while the RAC is dominated by macropores, indicating that the addition of recycled aggregates leads to more macropores and denser pores in the concrete under freeze–thaw cycles. From the concrete section diagram of PPF with different volume contents, it can be seen that when the volume content of PPF is 0.8%, the section is mainly composed of coarse pores, and the diameter of coarse pores is larger than that of other contents. When the volume content of PPF is 1.0%, it is also dominated by coarse pores, but the pores of the section are less, the pore distribution is more dispersed, and the proportion of white part of the section of $PV_{1.0}$ RAC is lower than that of RAC and NAC. When the volume content of PPF is 1.2%, the proportion of the white part of the specimen section is greater than that of $PV_{0.8}$ RAC and $PV_{1.0}$ RAC, and most of them are fine pores. It shows that in the freeze–thaw cycle environment, the proportion of pores in the section of recycled concrete increases first and then decreases with the increase of PPF content, and when the volume content of PPF is 1.0%, it is beneficial to resist the increase of pores in RAC. From the cross-section of concrete mixed with different volume contents of nano-TiO_2, it can be seen that when the volume content of nano-TiO_2 is 0.4%, the pores of the section are less, mainly coarse pores, and the pore distribution is more dispersed. The proportion of the white part of the section of $TV_{0.4}$ RAC is lower than that of RAC and NAC. When the volume content of nano-TiO_2 is 0.8%, the pores of the section are less, mainly coarse pores, but the diameter of the coarse pores is smaller than that of the $TV_{0.4}$RAC section. When the volume content of nano-TiO_2 is 1.2%, the proportion of the white part of the specimen section is much larger than that of $TV_{0.4}$RAC and $TV_{0.8}$RAC, which is dominated by fine pores, but the diameter of the accompanying coarse pores is the largest, indicating that under the freeze–thaw cycle environment, the proportion of pores in the recycled concrete section increases with the increase of nano-TiO_2 content. When the volume content of nano-TiO_2 is 0.4%, it is beneficial to resist the increase of pores in RAC. This is because the particle size of nano-TiO2 dioxide is small, and the incorporation of nano-TiO2 into concrete can optimize the pore distribution and reduce harmful pores, so improving the microstructure of concrete is better than PPF.

2.4.5 Elastic Modulus and Mechanism Analysis of RAC After Carbonization

After the freeze–thaw cycle, there will be some changes in the recycled concrete specimen, such as loose structure, larger holes, and extended cracks. These changes will lead to a change in the elastic modulus of recycled concrete. Compared with the static elastic modulus, the determination of the dynamic elastic modulus does not need to analyze the loading and constitutive relationship. It can be measured only by the dynamic elastic modulus tester, which is more energy-saving and convenient. Therefore, the change in the elastic modulus of recycled concrete can be used as an index to reflect the influence of the freeze–thaw cycle on the internal structure of recycled concrete. The dynamic elastic modulus of $100 \times 100 \times 400$ mm prism specimens after different freeze–thaw cycles are measured. The results of each specimen are shown in Table 6. From Table 6, when the specimen is not freeze-thawed, with the incorporation of recycled coarse aggregate, the dynamic elastic modulus of concrete decreases, which is 2.3GPa less than NAC. When adding different volume content of PPF, the dynamic elastic modulus of RAC has different degrees of

Table 6 Dynamic elastic modulus under different freeze–thaw cycles

No	Dynamic elastic modulus under different freeze–thaw cycles / GPa							
	0 times	S-D	50 times	S-D	100 times	S-D	150 times	S-D
NAC	38.30	1.473	36.49	1.827	36.39	0.694	36.21	1.428
RAC	36	1.671	33.93	1.456	33.7	1.730	32.56	1.671
$P_{V0.8}$RAC	37.12	1.922	34.15	1.341	32.67	1.832	31.18	1.447
$P_{V1.0}$RAC	38	1.649	34.96	1.115	33.44	1.628	31.92	1.755
$P_{V1.2}$RAC	37.18	1.653	34.21	1.716	32.72	1.163	31.23	1.692
$T_{V0.4}$RAC	34.85	1.774	32.74	1.927	32.33	2.031	31.01	1.465
$T_{V0.8}$RAC	36.22	1.832	33.54	0.937	33.22	1.052	31.99	1.629
$T_{V1.2}$RAC	34.63	1.529	32.8	1.572	32.48	1.174	32.12	1.927

Wei *et al. Int J Concr Struct Mater*   (2024) 18:28

Page 12 of 22
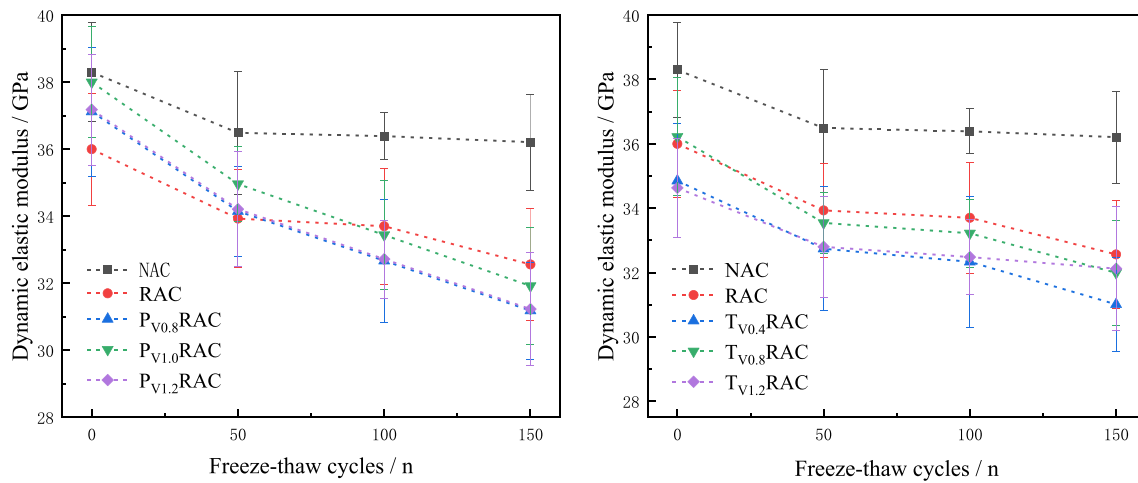
Fig. 12 Variation trend of dynamic elastic modulus of RAC

improvement. When the volume content of PPF is 1.0%, the $PV_{1.0}RAC$ has the best improvement, which is 2GPa higher than that of RAC. When adding different volume content of nano-TiO_2, the dynamic elastic modulus of RAC is reduced as a whole.

From Table 6, the variation trend of dynamic elastic modulus of concrete specimens with the increase of freeze–thaw cycles under different volume contents of nano-TiO2 and PPF is obtained, as shown in Fig. 12. From Fig. 12, the dynamic elastic modulus of NAC is the best under different freeze–thaw cycles. When the number of freeze–thaw cycles is low, the dynamic elastic modulus of RAC mixed with PPF decreases more slowly, indicating that PPF is more suitable than nano-TiO_2 to protect the internal structure of RAC and improve the frost resistance of RAC at low freeze–thaw cycles, and PPF has the best volume content (1.0%). When the number of freeze–thaw cycles is high, the protection degree of nano-TiO_2 on the internal structure of RAC is slightly higher than that of PPF. From Fig. 12, when the number of freeze–thaw cycles is 150 times and the volume content of nano-TiO_2 is 0.8 and 1.2%, the dynamic elastic modulus of RAC is higher than that of PPF, indicating that with the increase of the number of freeze–thaw cycles, the protective effect of nano-TiO_2 on the internal structure of RAC also increases. This is because nano-TiO_2 is an inert material and has a filling effect. In the case of increasing freeze–thaw cycles, it can still improve the frost resistance of concrete. Therefore, compared with PPF, nano-TiO_2 has better protection for the internal structure of concrete under higher freeze–thaw cycles.

3 Analysis of Frost Resistance and Carbonation Resistance of Specimens Based on Model

3.1 RAC Freeze–Thaw Damage Model and Carbonation Model Based on RSM

Response surface methodology (RSM) is a comprehensive experimental technique based on statistics and experimental data. It is suitable for dealing with the effect of multiple variables on a system or structure (Köksal et al., 2022; Shi et al., 2022; Ghafari et al., 2023). In this section, the mechanical properties model, elastic modulus model, and carbonation depth model were established by RSM. The effects of freeze–thaw cycles, nano-TiO_2, and PPF volume content on the frost resistance of RAC and the effects of carbonation days, nano-TiO2, and PPF volume content on the carbon resistance of RAC were analyzed. The multiple regression equations and coefficients of each model are shown in Table 7. The multiple regression equations and coefficients are shown in Table 7. The P values of all models in the table are < 0.0001, indicating that the correlation of the model is significant. The coefficient of variation C.V value is small, indicating that the reliability of the model is relatively high. The R^2 of the model is close to 1, indicating that the model fit was good.

3.2 Analysis of Frost Resistance and Carbonation Resistance

3.2.1 RAC Mechanical Properties Damage Model on RSM

The compressive strength model and splitting tensile strength model of RAC with different volume contents of nano-TiO_2 and PPF after freeze–thaw cycles were

Table 7 Multiple regression equation and coefficient

| Model type	Multivariate regression equation	P	C.V/%	R^2
Compressive strength	$F_{Tc} = 57.00341 - 0.033589A - 18.34818B$	<0.0001	0.93	0.9960
	$-2.9125 \times 10^{-3}AB - 3.353 \times 10^{-4}A^2 + 6.2267B^2$			
	$F_{Pc} = 36.32011 - 0.0589A + 29.77B$	<0.0001	1.69	0.9798
	$-0.0475AB + 9.52 \times 10^{-5}A^2 - 17.80172B^2$			
Splitting tensile strength	$F_{Tf} = 3.11724 + 6.614 \times 10^{-3}A - 0.34828B$	<0.0001	5.17	0.8892
	$+8.75 \times 10^{-4}AB - 7.21 \times 10^{-5}A^2 - 0.12608B^2$			
	$F_{PS} = -4.80690 - 0.021931A + 19.0431B$	<0.0001	4.20	0.9356
	$+0.025AB - 5.03 \times 10^{-5}A^2 - 10.64655B^2$			
Dynamic elastic modulus increment	$D_T = 30.88 + 0.0043A + 6.3375B$	<0.0001	0.43	0.9773
	$+0.013125AB - 1.4 \times 10^{-4}A^2 - 4.4375B^2$			
	$D_P = 17.61868 - 0.02962A + 37.46868B$	<0.0001	0.043	0.9999
	$-2.5 \times 10^{-4}AB - 4.82759 \times 10^{-7}A^2 - 18.65517B^2$			
Carbonation depth	$C_T = 3.03764 + 0.23549A - 5.16746B$	<0.0001	5.26	0.9242
	$+9.82 \times 10^{-3}AB - 3.14 \times 10^{-3}A^2 + 2.83513B^2$			
	$C_P = 19.31859 + 0.18675A - 39.78578B$	<0.0001	5.69	0.9803
	$-0.020663AB - 3.14 \times 10^{-3}A^2 + 20.34914B^2$			

obtained by RSM. The three-dimensional response surface and heat maps of the compressive strength and splitting tensile strength of RAC under freeze–thaw cycles were obtained by Design Expert software to analyze the significance of the effects of nano-TiO$_2$, PPF and the number of freeze–thaw cycles on the compressive strength and splitting tensile strength of RAC, as shown in Figs. 13, 14a, b.

From Fig. 13a, the three-dimensional surface of RAC compressive strength decreases with the increase of freeze–thaw cycles, and the surface of RAC compressive strength with nano-TiO$_2$ is steeper along the direction of freeze–thaw cycles. The three-dimensional surface of RAC compressive strength decreases first and then increases with the increase of nano-TiO$_2$ volume content, and increases first and then decreases with the increase of PPF volume content. The decrease rate of RAC compressive strength with the increase of nano-TiO$_2$ and PPF volume content is lower than that with the increase of freeze–thaw cycles, indicating that the effect of freeze–thaw cycles on RAC compressive strength is more intense. Compared with the two compressive strength surfaces mixed with nano-TiO2 and PPF, the reduction of compressive strength is roughly similar, but when the number of freeze–thaw cycles is large, the volume content of PPF is 1.0%, which has a better effect on the frost resistance of RAC than nano-TiO$_2$.

From Fig. 13b, with the increase of freeze–thaw cycles, the three-dimensional surface of RAC splitting tensile strength decreases, and the compressive strength surface

with PPF is steeper along the direction of freeze–thaw cycles. The three-dimensional surface of RAC splitting tensile strength decreases with the increase of nano-TiO$_2$ volume content, and nano-TiO$_2$ with small volume content is more suitable for the improvement of RAC frost resistance. The three-dimensional surface of RAC splitting tensile strength increases first and then decreases with the increase of PPF volume content, and the RAC splitting tensile strength is larger when the PPF volume content is 1.0%. The rate of decrease of RAC splitting tensile strength with the increase of nano-TiO2 volume content is lower than that with the increase of freeze–thaw cycles. The RAC splitting tensile strength increases first and then decreases with the increase of PPF volume content, indicating that PPF is more conducive to the improvement of RAC splitting tensile strength under freeze–thaw cycles, and there is an optimal volume content (1.0%).

From Fig. 14a, the bending direction of RAC contour lines mixed with nano-TiO2 and PPF is opposite. The bending direction of RAC contour lines mixed with nano-TiO$_2$ is lower to the left, while the bending direction of RAC contour lines mixed with PPF is higher to the right, indicating that under freeze–thaw conditions, PPF has a higher protective effect on the compressive strength of RAC than nano-TiO$_2$. The density of the ordinate contour lines of the two contour maps is similar, indicating that under the same number of freeze–thaw cycles, nano-TiO$_2$ and PPF have similar effects on the compressive strength of RAC, but the incorporation of
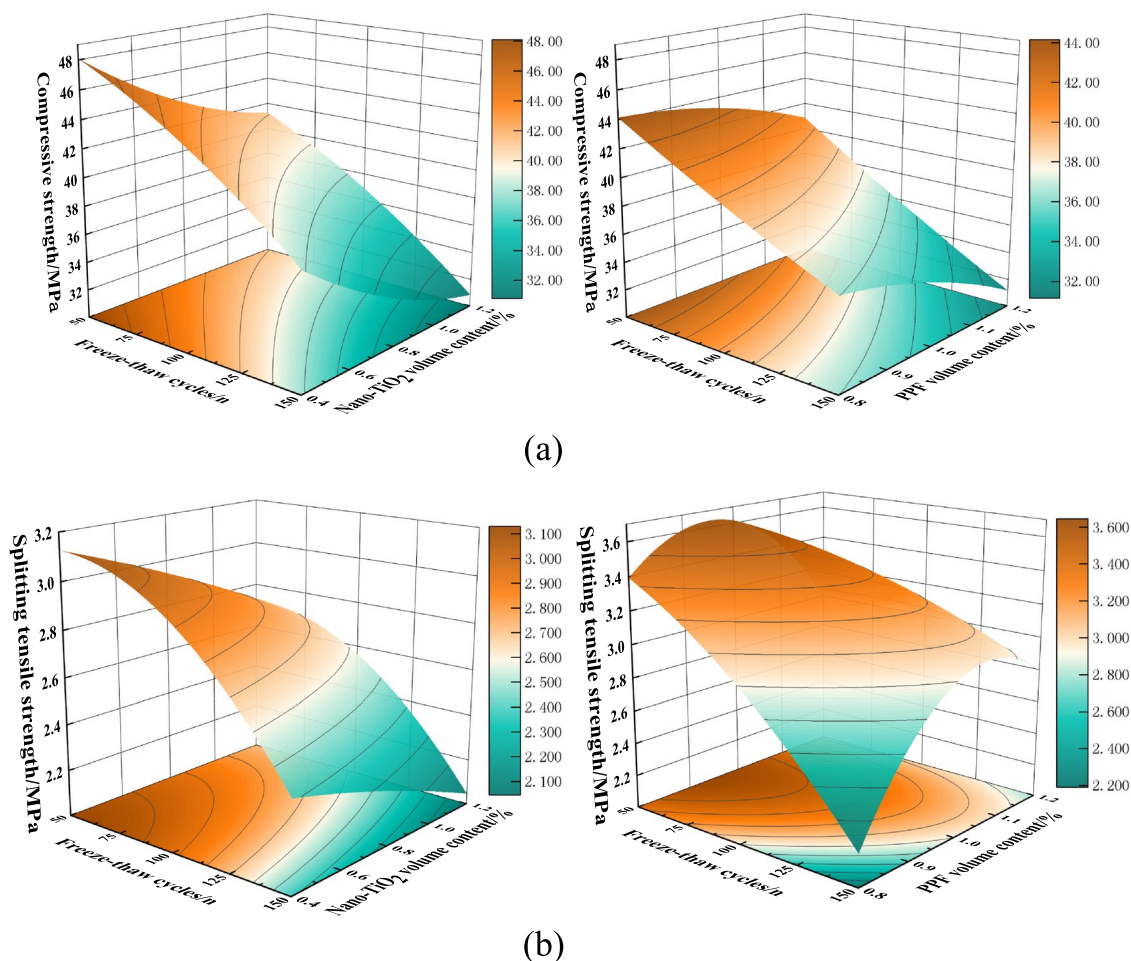
Fig. 13 **a** Response surface of compressive strength of PPF and nano-TiO$_2$ with different volume fractions. **b**. Response surface of splitting tensile strength of PPF and nano-TiO$_2$ with different volume fractions

PPF is more suitable for improving the frost resistance of RAC, and both of them are nano-TiO$_2$ and PPF. When the content is low, the frost resistance of RAC compressive strength is better.

From Fig. 14b, the bending direction of the RAC contour lines doped with nano-TiO$_2$ and PPF is the same, but the density of the RAC ordinate contour lines doped with nano-TiO$_2$ is lower than that of the RAC ordinate contour lines doped with PPF, and the orange range of the RAC contour lines doped with PPF is larger, indicating that the effect of PPF on the splitting tensile strength of RAC under freeze–thaw environment is greater than that of nano-TiO$_2$ on the splitting tensile strength of RAC, and the protective effect of PPF on the splitting tensile strength of RAC is higher than that of nano-TiO$_2$. When the volume content of PPF is 1.0%, the frost resistance of RAC splitting tensile strength is better.

3.2.2 RAC Elastic Modulus Damage Model on RSM

The dynamic elastic modulus model of RAC with different volume contents of nano-TiO$_2$ and PPF after freeze–thaw cycles were obtained by RSM. The three-dimensional response surface and heat maps of the dynamic elastic modulus of RAC under freeze–thaw cycles were obtained by Design Expert to analyze the significance of the effects of nano-TiO$_2$, PPF and the number of freeze–thaw cycles on the dynamic elastic modulus of RAC, as shown in Fig. 15a, b.
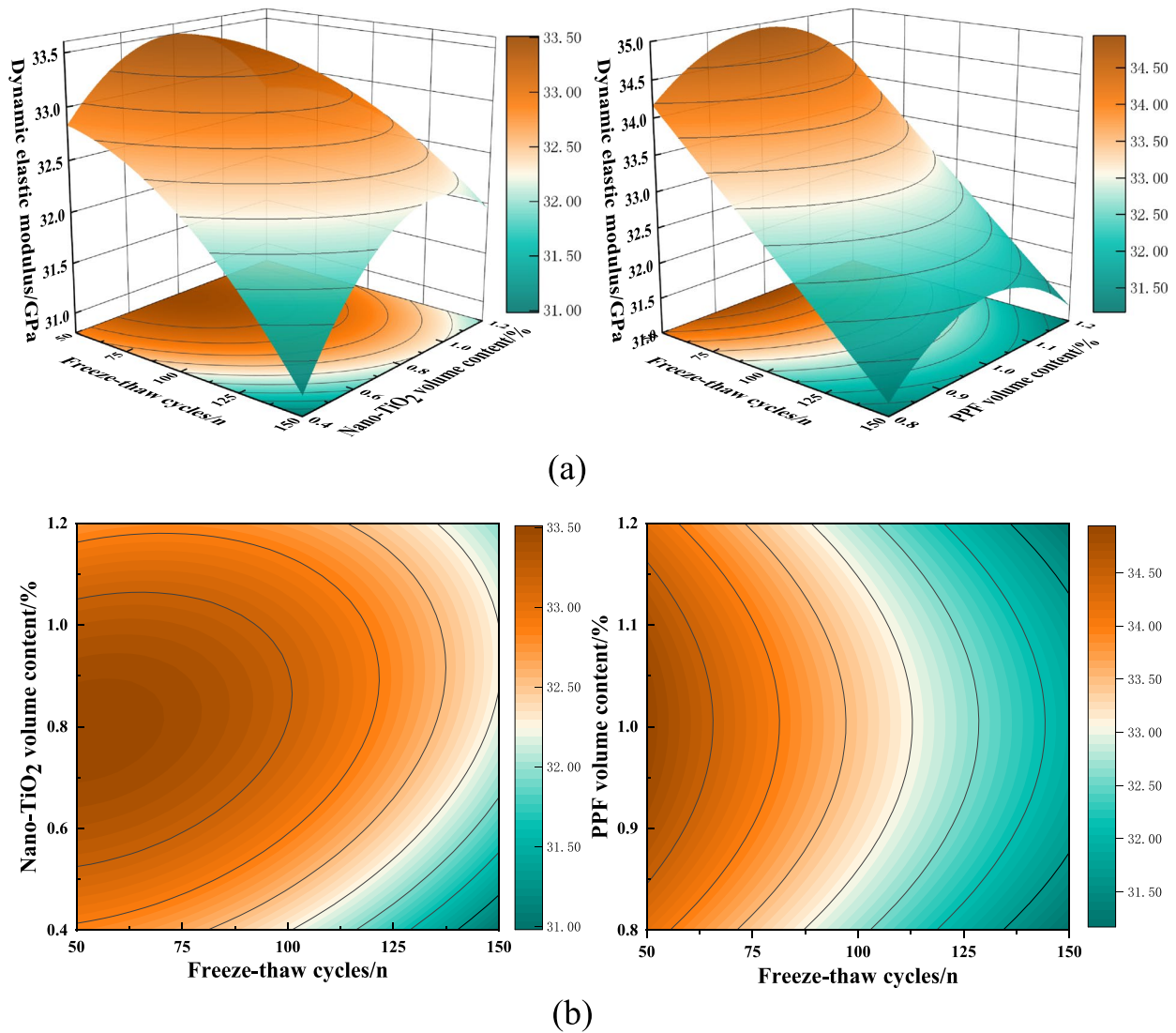
From Fig. 15a, the dynamic elastic modulus of RAC with different volume fractions of nano-TiO$_2$ and PPF decreases with the increase of freeze–thaw cycles, and the RAC surface with PPF is steeper along the direction of the increase of freeze–thaw cycles, indicating that the initial defects of RAC will increase during the freeze–thaw cycle, accelerating the speed and degree of internal

(a)

(b)
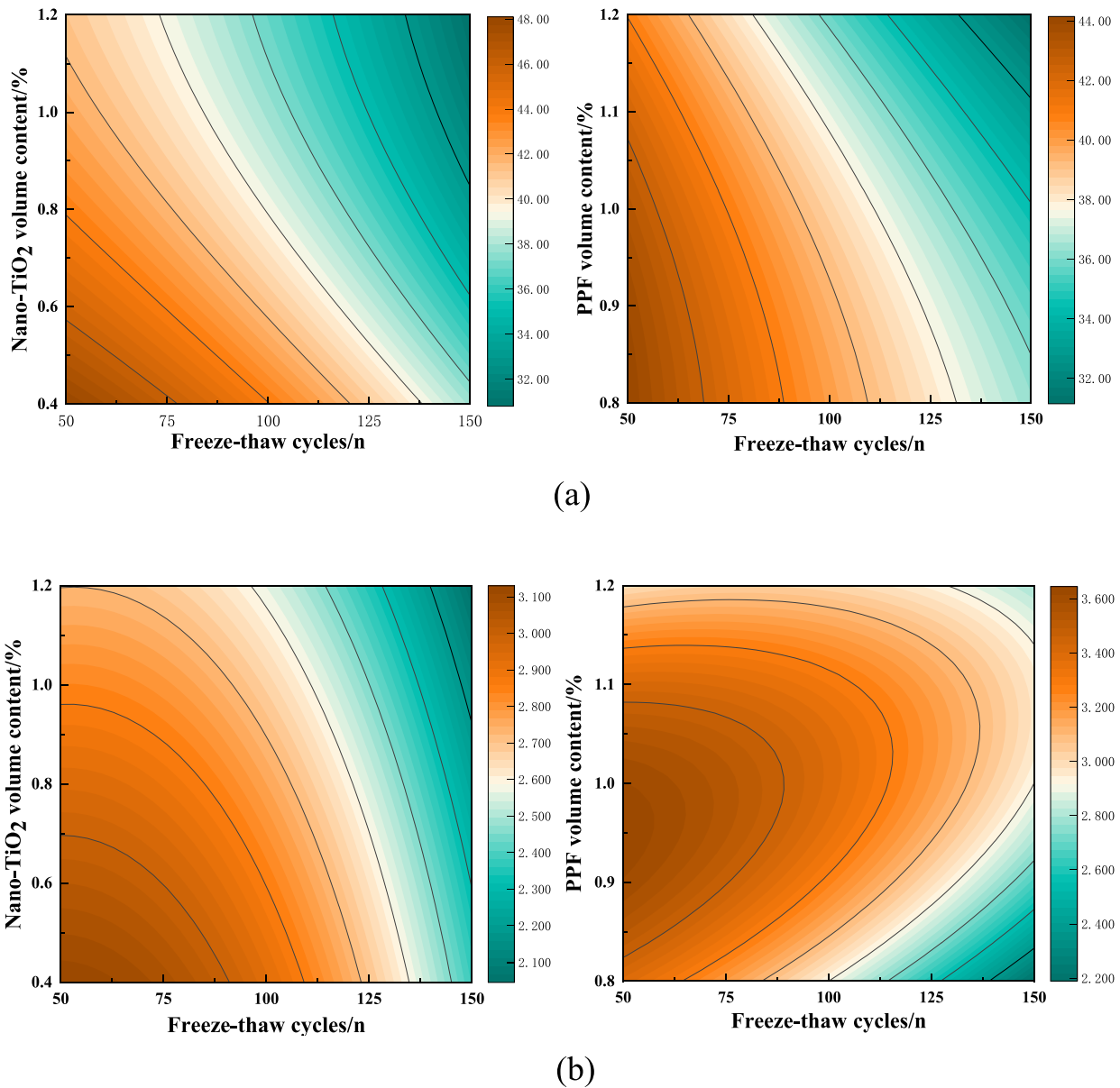
Fig. 14 **a** Contour map of compressive strength of PPF and nano-TiO$_2$ with different volume fractions. **b** Contour map of splitting tensile strength of PPF and nano-TiO$_2$ with different volume fractions

structural cracking, while the effect of PPF on alleviating internal structural cracking is lower than that of nano-TiO$_2$. The incorporation of nano-TiO$_2$ can make the dynamic elastic modulus of RAC decrease more slowly in the freeze–thaw environment. When the number of freeze–thaw cycles is 150, the dynamic elastic modulus of RAC doped with nano-TiO2 is 1~2GPa higher than that of RAC doped with PPF. It shows that under freeze–thaw conditions, the incorporation of nano-TiO$_2$ and PPF can effectively improve the internal structure of recycled concrete and slow down the expansion of

internal pores. However, the overall improvement effect of nano-TiO$_2$ is better than that of PPF, and the RAC with 0.8% nano-TiO$_2$ content has the largest relative dynamic elastic modulus, slight internal deterioration and loose damage, and the best frost resistance. From Fig. 15b that the effects of nano-TiO2 and PPF on the dynamic elastic modulus of RAC are similar at lower freeze–thaw cycles. However, with the increase of freeze–thaw cycles, the effect of nano-TiO2 on the dynamic elastic modulus of RAC is higher than that of PPF, indicating that

(a)

(b)

Fig. 15 **a** Response surface of dynamic elastic modulus of PPF and nano-TiO$_2$ with different volume fractions. **b** Contour map of dynamic elastic modulus of PPF and nano-TiO$_2$ with different volume fractions

nano-TiO2 has a better positive effect on the frost resistance of RAC internal structure.

3.2.3 Carbonation Model Analysis of RAC

The carbonation depth model of RAC with different nano-TiO$_2$ and PPF volume content after different days of carbonization was obtained by RSM. The three-dimensional response surface and heat map of RAC carbonization depth under carbonization were obtained by Design Expert, and the significance of nano-TiO2, PPF and carbonization days on the carbon resistance of RAC was analyzed. As shown in Fig. 16a, b. And the carbonation

depth of the control group without nano-TiO$_2$ and PPF is 6.26 mm after 28 days of carbonation.

From Fig. 16a that the carbonation depth of RAC with different volume contents of nano-TiO$_2$ and PPF increases with the increase of carbonation days. The surface of RAC with nano-TiO$_2$ is steeper along the increase of carbonation days. The carbonation depth of RAC with nano-TiO$_2$ is 2–3 mm higher than that of PPF, and the carbonation depth of RAC with nano-TiO$_2$ and PPF is lower than that of the control group (6.26 mm) after 28 days of carbonation, indicating that the incorporation of nano-TiO$_2$ and PPF can improve the carbon resistance of RAC. However, the effect of PPF on alleviating

(a)

(b)
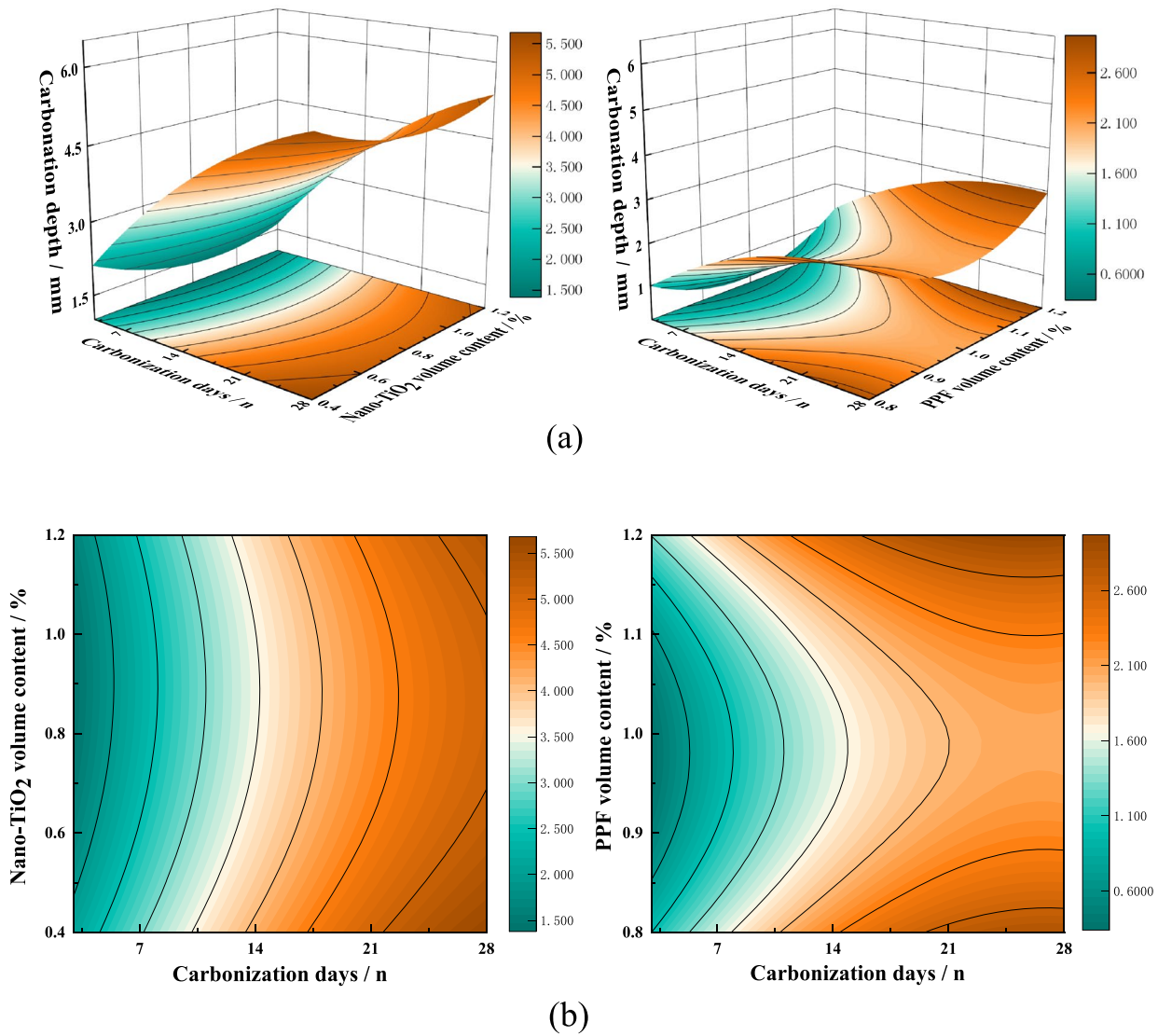
Fig. 16 a Response surface of carbonation depth of PPF and nano-TiO$_2$ with different volume fractions. **b** Contour map of carbonation depth of PPF and nano-TiO$_2$ with different volume fractions

the internal carbonation depth of RAC is higher than that of nano-TiO$_2$. Under the condition of the same carbonation days, the carbonation depth of RAC with nano-TiO$_2$ increases with the increase of volume content. When the volume content of nano-TiO$_2$ is 0.4%, the carbonation depth of RAC is the lowest, while the carbonation depth of RAC with PPF decreases first and then increases with the increase of volume content. When the volume content of PPF is 1.0%, the carbonation depth of RAC is the lowest and the carbon resistance is the best. From Fig. 16b, the contour density along the axis of nano-TiO$_2$ volume content is lower than that along the axis of PPF volume content, indicating that nano-TiO$_2$ has a lower degree of influence on the carbonation depth of RAC

than PPF, and PPF has a better positive effect on the carbon resistance of RAC.

3.3 Prediction of Optimal Values for Frost Resistance and Carbonation Resistance

The mechanical properties model, dynamic elastic modulus model, and carbonation depth model obtained by RSM are used to predict the experimental values under different freeze–thaw times and carbonation days. The predicted values are shown in Tables 8, 9. From Table 9, the 3D scatter diagram of the error between the true value and the predicted value of the dynamic elastic modulus and the carbonation depth can be obtained, as shown in Fig. 18a, b.

From Fig. 17 that the error range of compressive strength is less than 1.0, and the error range of splitting tensile strength is less than 0.5. Combined with the P value, C.V value, and R^2 obtained by the RSM model, it shows that the model prediction has good reliability and significant correlation. From Fig. 17a, the error range of compressive strength of RAC mixed with nano-TiO_2 is relatively concentrated, and the overall error range is smaller than that of PPF. From Fig. 17b, the error range of splitting tensile strength of RAC mixed with nano-TiO_2 and PPF is relatively dispersed, and the overall error range is similar. The results show that the RSM model of RAC mixed with nano-TiO_2 is more suitable for the prediction of compressive strength and splitting tensile strength, and the prediction reliability is better.

From Fig. 18 that the error range of dynamic elastic modulus is less than 0.2, and the error range of carbonization depth is less than 1. Combined with the P value, C.V value, and R^2 obtained by the RSM model, it shows that the model prediction has good reliability and significant correlation. From Fig. 18a that the error range of the dynamic elastic modulus of PPF is relatively concentrated, and the overall error range is smaller than that of nano-TiO_2. From Fig. 18b that the error range of carbonation depth of PPF is relatively concentrated, and the overall error range is smaller than that

of nano-TiO_2. The results show that the RSM model of RAC with PPF is more suitable for the prediction of dynamic elastic modulus and carbonation depth, and the prediction reliability is better.

4 Conclusion

1) When the PPF volume content is 1.2%, the compressive strength of $PV_{1.2}RAC$ reaches the maximum (46 MPa), and compared with the control group NAC and RAC, the compressive strength decreased by 11.8 and 7.2%, respectively. When the volume content of PPF is 1.0%, the splitting tensile strength of $PV_{1.0}RAC$ reaches the maximum (3.7 MPa), and compared with the control group NAC and RAC, the splitting tensile strength increases by 12.1 and 15.6%, respectively. When the nano-TiO_2 volume content is 0.4%, the compressive strength of $TV_{0.4}RAC$ reaches the maximum (49.8 MPa), and compared with the control group NAC and RAC, the compressive strength is reduced by 4.5 and − 0.4%, respectively. When the volume fraction of nano-TiO_2 is 0.8%, the splitting tensile strength of $TV_{0.8}RAC$ reached the maximum (3.4 MPa), and compared with the control group NAC and RAC, the splitting tensile strength increased by 3 and 6%, respectively. It shows that PPF

Table 8 Test value and predicted value of mechanical properties

No	Compressive strength/MPa						Splitting tensile strength/MPa					
	50		100		150		50		100		150	
	T-V	P-V	T-V	P-V	T-V	P-V	T-V	P-V	T-V	P-V	T-V	P-V
$P_{V0.8}RAC$	43.4	44.14	40.9	40.01	36.2	36.35	3.3	3.39	3.1	2.92	2.7	2.20
$P_{V1.0}RAC$	44.3	43.41	38.4	38.60	34.4	34.47	3.6	3.62	3.4	3.39	2.9	2.92
$P_{V1.2}RAC$	40.5	40.85	35.9	35.77	31.4	31.17	3.1	2.99	2.8	3.01	2.9	2.80
$T_{V0.4}RAC$	48.2	48.08	43.8	43.83	37.9	37.90	2.9	3.13	2.6	2.93	2.2	2.38
$T_{V0.8}RAC$	43.7	43.68	39.3	39.37	33.8	33.38	3.2	2.94	2.8	2.77	2.5	2.33
$T_{V1.2}RAC$	41.0	41.26	37.5	36.89	30.4	30.25	3.0	2.72	2.7	2.56	2.3	2.05

Table 9 Test value and predicted value of dynamic elastic modulus and carbonation depth

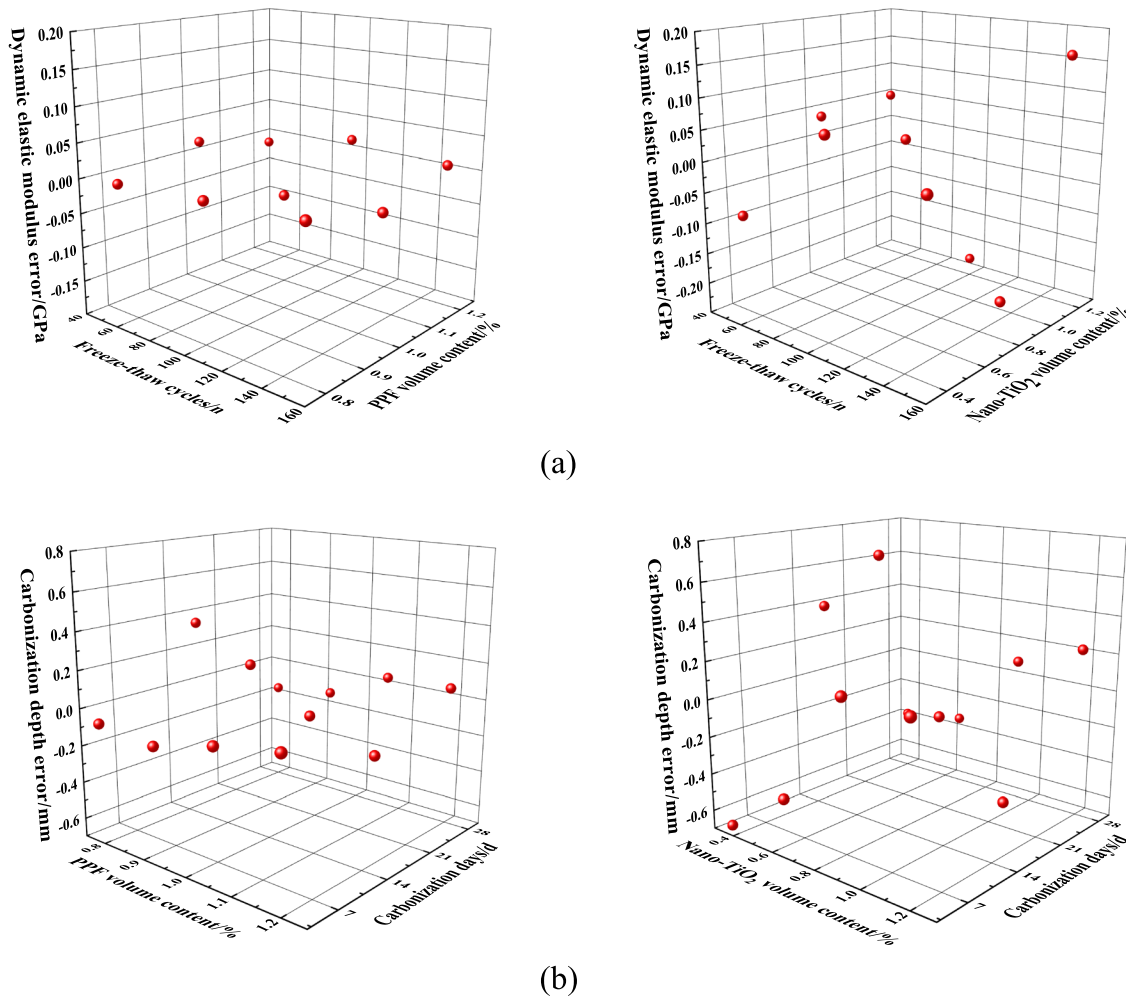| No	Dynamic elastic modulus/GPa						Carbonation depth/mm							
	50		100		150		3		7		14		28	
	T-V	P-V	T-V	P-V	T-V	P-V	T-V	P-V	T-V	P-V	T-V	P-V	T-V	P-V
$P_{V0.8}RAC$	34.15	34.16	32.67	32.67	31.18	31.17	0.95	1.00	1.47	1.55	2.29	2.28	2.89	2.82
$P_{V1.0}RAC$	34.96	34.94	33.44	33.47	31.92	31.94	0.71	0.35	1.08	0.89	1.58	1.59	1.94	2.07
$P_{V1.2}RAC$	34.21	34.22	32.72	32.70	31.23	31.22	1.19	1.34	1.75	1.86	2.58	2.53	3.01	2.95
$T_{V0.4}RAC$	32.74	32.83	32.33	32.26	31.01	30.99	1.47	2.11	2.56	2.95	4.36	4.16	5.85	5.66
$T_{V0.8}RAC$	33.54	33.50	33.22	33.19	31.99	32.18	1.82	1.42	2.97	2.26	3.45	3.51	4.66	5.07
$T_{V1.2}RAC$	32.8	32.75	32.48	32.70	32.12	31.96	1.26	1.63	2.18	2.50	3.86	3.77	5.6	5.38

(a)

(b)
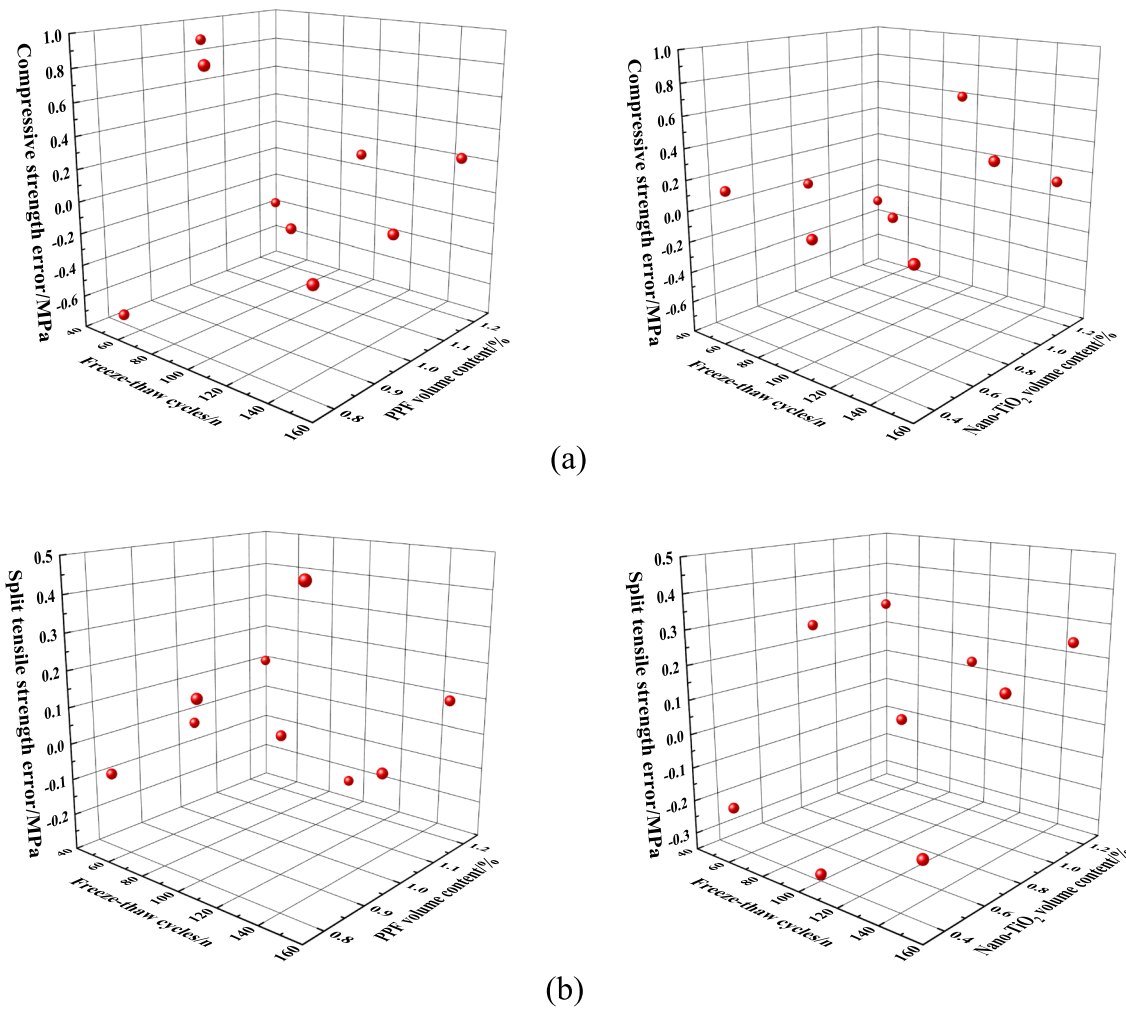
Fig. 17 **a** Compressive strength error 3D scatter plot. **b** Split tensile strength error 3D scatter plot

is more suitable for the improvement of RAC splitting tensile strength, and nano-TiO$_2$ material is more suitable for the improvement of RAC compressive strength.

2) The contribution rate of RAC compressive strength decreases with the increase of nano-TiO$_2$ and PPF content, and the contribution rate of splitting tensile strength increases first and then decreases with the increase of nano-TiO$_2$ and PPF content. When the number of freeze–thaw cycles is large, the contribution rate of nano-TiO$_2$ to the compressive strength of RAC is better, and the contribution rate of PPF to the splitting tensile strength of RAC is better, indicating that nano-TiO$_2$ is more conducive to improving the frost resistance of RAC compressive strength, and PPF is more conducive to improving the frost resistance of RAC splitting tensile strength. The contribution rates of nano-TiO$_2$ and PPF with different volume contents to the mechanical properties of RAC have optimal values, which are 0.4 and 1.0%, respectively.

3) Under freeze–thaw conditions, nano-TiO$_2$ and PPF incorporation can effectively inhibit the loss of RAC quality and the generation of pores. When the volume content of nano-TiO$_2$ is 0.4 and 1.2%, the mass loss is 1 and 0.8%, respectively, and the frost resistance is better. When the volume content of nano-TiO$_2$ is 0.4%, the internal voids of TV$_{0.4}$RAC are lower than those of RAC and NAC in the control group, and the effect of inhibiting pore increase is better than that of PPF. When the volume content of nano-TiO$_2$ is 0.8 and 1.2%, the dynamic elastic modulus of TRAC is higher than that of PRAC, indicating that nano-TiO$_2$ plays a better protective role in the internal structure of RAC. The incorporation of nano-TiO$_2$ and PPF can improve the carbon resist-

(a)

(b)

Fig. 18 **a** Dynamic elastic modulus error 3D scatter plot. **b** Carbonization depth error 3D scatter plot

ance of RAC. When the volume content of nano-TiO$_2$ is 0.4%, TV$_{0.4}$RAC has the lowest carbonation depth and the best carbon resistance. When the volume content of PPF is 1.0%, PV$_{1.0}$RAC has the lowest carbonation depth and the best carbon resistance.

4) The RSM model of RAC durability is significant, and the fitting degree is good and the accuracy is high. The error range between the predicted compressive strength and the experimental value is less than 1.0 MPa, and the error range between the predicted splitting tensile strength and the experimental value is less than 0.5 MPa. The RSM model of RAC with nano-TiO$_2$ is more suitable for the prediction of compressive strength and splitting tensile strength. The error range between the predicted dynamic elastic modulus and the experimental value is less than

0.2 GPa, and the error range between the predicted carbonation depth and the experimental value is less than 1 mm. The RSM model of RAC with PPF is more suitable for the prediction of dynamic elastic modulus and carbonation depth.

5) In this paper, green recycled concrete materials are developed by using nano-materials and fiber materials, respectively, which has certain guiding significance for the promotion of low-carbon green concept, artificial sand, fiber and nano-materials in engineering practice. In this paper, the optimum content of PPF of nano-TiO$_2$ in the preparation of concrete is obtained. On this basis, the properties (such as fatigue life) of different RCA substitution rates (25, 75 and 100%) can be further studied.

Abbreviations

PPF	Polypropylene fiber
RAC	Recycled concrete
NAC	Natural concrete
PRAC	Polypropylene fiber recycled concrete
TRAC	Nano-TiO2 recycled concrete
IOT	High-iron tailings
RSM	Response surface methodology
MS	Manufactured sand
NS	Natural sand
CO2	Carbon dioxide
SD	Standard deviations
A	The number of freeze–thaw cycles(mechanical properties model)/ The number of carbonation days(carbonation depth model)
B	The volume content of nano-TiO2 (PPF)
T-V	Strength experimental value
P-V	Strength predicted value
Qc,V	The contribution rate of nano-TiO2 and PPF to compressive strength
Qt,V	The contribution rate of nano-TiO2 and PPF to splitting tensile strength

Availability of data and materials
All data generated or analyzed during this study are included in this published article.

Declarations

Ethics approval and consent to participate
Not applicable.

Consent for publication
Not applicable.

Competing interests
The authors declare that they have no competing interests.

References

Aghajanian, A., Cimentada, A., Behfarnia, K., Brand, A. S., & Thomas, C. (2023). Microstructural analysis of siderurgical aggregate concrete reinforced with fibers. *Journal of Building Engineering*, *64*, 105543. https://doi.org/10.1016/j.jobe.2022.105543

Ahdal, Q. A., Amrani, A. M., Ghaleb, A. A. A., Abadel, A. A., Alghamdi, H., Alamri, M., Wasim, M., & Shameeri, M. (2022). Mechanical performance and feasibility analysis of green concrete prepared with local natural zeolite and waste PET plastic fibers as cement replacements. *Case Studies in Construction Materials*, *17*, e01256. https://doi.org/10.1016/j.cscm.2022.e01256

Ahmed, Hussein Twana, Hunar, Dheyaaldin Mahmood, Ali, Mosaberpanah Mohammad, Ahmed Younus, M. S., Mohammed Hariwan, A., Omer Raian, R., Hamid Saad, M., & Radhwan, Alzeebaree. (2023). Chemical resistance of alkali-activated mortar with nano silica and polypropylene fiber. *Construction and Building Materials*. https://doi.org/10.1016/j.conbuildmat.2022.129847

Alashker, Y., & Raza, A. (2022). Seismic performance of recycled aggregate geopolymer concrete-filled double skin tubular columns with internal steel and external FRP tube. *Polymers*, *14*(23), 5204. https://doi.org/10.3390/polym14235204

Ali, Memon Shazim, Zere, Bekzhanova, & Aray, Murzakarimova. (2022). A review of improvement of interfacial transition zone and adherent mortar in recycled concrete aggregate. *Buildings*. https://doi.org/10.3390/buildings12101600

Awoyera, P. O., Effiong, J. U., Olalusi, O. B., Prakash Arunachalam, K., de Azevedo, A. R. G., Martinelli, F. R. B., et al. (2022). Experimental findings and validation on torsional behaviour of fibre-reinforced concrete beams: a review. *Polymers*, *14*(6), 1171. https://doi.org/10.3390/polym14061171

Bamigboye, G. O., Okechukwu, U. E., Olukanni, D. O., Bassey, D. E., Okorie, U. E., Adebesin, J., & Jolayemi, K. J. (2022). Effective economic combination of waste seashell and river sand as fine aggregate in green concrete. *Sustainability*, *14*(19), 12822. https://doi.org/10.3390/su141912822

Deng, Q., Zhang, R., Liu, C., Duan, Z., & Xiao, J. (2023). Influence of fiber properties on abrasion resistance of recycled aggregate concrete: length, volume fraction, and types of fibers. *Construction and Building Materials*, *362*, 129750. https://doi.org/10.1016/j.conbuildmat.2022.129750

Elsayed, M., Abd-Allah, S. R., Said, M., & El-Azim, A. A. (2023). Structural performance of recycled coarse aggregate concrete beams containing waste glass powder and waste aluminum fibers. *Case Studies in Construction Materials*, *18*, e01751. https://doi.org/10.1016/j.cscm.2022.e01751

Erfan, Najaf, Maedeh, Orouji, & Mehdi, Zahrai Seyed. (2022). Improving nonlinear behavior and tensile and compressive strengths of sustainable lightweight concrete using waste glass powder, nanosilica, and recycled polypropylene fiber. *Nonlinear Engineering*. https://doi.org/10.1515/nleng-2022-0008

Feng, C., Cui, B., Huang, Y., et al. (2022). Enhancement technologies of recycled aggregate–enhancement mechanism, influencing factors, improvement effects, technical difficulties, life cycle assessment. *Construction and Building Materials, 317*, 126168.

Ghafari, S., et al. (2023). Sustainable crumb rubber modified asphalt mixtures based on low-temperature crack propagation characteristics using the response surface methodology. *Theoretical and Applied Fracture Mechanics*, *123*, 103718. https://doi.org/10.1016/j.tafmec.2022.103718

GB/T50082–2009, Standard for test methods of long-term performance and durability of ordinary concrete[S].

GB/T50081–2019, Standard for test method of mechanical properties of ordinary concrete[S].

GB 50204–2002. (2011). Code for acceptance of constructional quality of concrete structure[S].

Hassan, A., Farhan, A., & Muhammad, Q. I. (2023). Enhanced mechanical and durability resilience of plastic aggregate concrete modified with nano-iron oxide and sisal fiber reinforcement. *Construction and Building Materials*. https://doi.org/10.1016/j.conbuildmat.2023.132911

Hui-lin, Xue, et al. (2022). Improving mechanical properties of manufactured sand concrete with high biotite content: application of magnetic separation process and equipment optimization. *Construction and Building Materials*. https://doi.org/10.1016/j.conbuildmat.2022.128861

Hunar, Dheyaaldin Mahmood, Ali, Mosaberpanah Mohammad, & Radhwan, Alzeebaree. (2022). The effect of nano-silica and nano-alumina with polypropylene fiber on the chemical resistance of alkali-activated mortar. *Sustainability*. https://doi.org/10.3390/su142416688

JGJ 55–2011, Specification for mix proportion design of ordinary concrete[S].

Jiale, Wu., et al. (2022). Particle characterization of manufactured sand and its influence on concrete properties. *Materials, 15*(13), 4593–4593.

Köksal, F., Beycioğlu, A., & Dobiszewska, M. (2022). Optimization based on toughness and splitting tensile strength of steel-fiber-reinforced concrete incorporating silica fume using response surface method. *Materials*, *15*(18), 6218. https://doi.org/10.3390/ma15186218

Kun, Wang, Jinjun, Guo, Peng, Zhang, & Qingxin, Meng. (2022). The counterbalance of the adverse effect of abrasion on the properties of concrete incorporating nano-SiO2 and polypropylene fiber based on pore structure fractal characteristics. *Fractal and Fractional*. https://doi.org/10.3390/fractalfract6070392

Li, C., Liu, T., Fu, H., Zhang, X., Yang, Y., & Zhao, S. (2021). Test and evaluation of the flexural properties of reinforced concrete beams with 100% recycled coarse aggregate and manufactured sand. *Buildings*, *11*(9), 420. https://doi.org/10.3390/buildings11090420

Wei *et al. Int J Concr Struct Mater*   (2024) 18:28

Page 22 of 22

Liang, Zhiu, Zhiheng, Hu., Yingwu, Zhou, Yufei, Wu., Xiaoqing, Zhou, Biao, Hu., & Menghuan, Guo. (2022). Improving recycled aggregate concrete by compression casting and nano-silica. *Nanotechnology Reviews*. https://doi.org/10.1515/ntrev-2022-0065

Liu, S., Zhang, Y., Liu, B., Zou, Z., Liu, Q., Teng, Y., et al. (2022). Sustainable use of waste oyster shell powders in a ternary supplementary cementitious material system for green concrete. *Materials*, *15*(14), 4886. https://doi.org/10.3390/ma15144886

Marta, Ka. łuża. (2022). Experimental analysis of surface application of fiber-reinforced polymer composite on shear behavior of masonry walls made of autoclaved concrete blocks. *Buildings*. https://doi.org/10.3390/buildings12122208

Marwan, H. A., Muyideen, A., TJ, M., et al. (2022). Mechanical properties of concrete containing recycle concrete aggregates and multi-walled carbon nanotubes under static and dynamic stresses. *Case Studies in Construction Materials*. https://doi.org/10.1016/j.cscm.2022.e01651

Nafees, A., Amin, M. N., Khan, K., Nazir, K., Ali, M., Javed, M. F., et al. (2021). Modeling of mechanical properties of silica fume-based green concrete using machine learning techniques. *Polymers*, *14*(1), 30. https://doi.org/10.3390/polym14010030

Nattapong, Damrongwiriyanupap, Akaraphol, Wachum, Kamonphop, Khansamrit, Satakhun, Detphan, Sakonwan, Hanjitsuwan, Tanakorn, Phoongernkham, Piti, Sukontasukkul, yuan, Li Long, & Prinya, Chindaprasirt. (2021). Improvement of recycled concrete aggregate using alkali-activated binder treatment. *Materials and Structures*. https://doi.org/10.1617/s11527-021-01836-1

Qin, Y., Li., Y., Zhang, W., & Zhou, H. (2022). Constitutive model of polypropylene-fiber-fabric-reinforced concrete under uniaxial compression and index conversion of mechanical properties. *Construction and Building Materials*, *347*, 128508. https://doi.org/10.1016/j.conbuildmat.2022.128508

Qiuhong, Zhao, Youqun, Wang, Meng, Xie, & Baoshan, Huang. (2022). Experimental study on mechanical behavior of steel fiber reinforced geopolymeric recycled aggregate concrete. *Construction and Building Materials*. https://doi.org/10.1016/j.conbuildmat.2022.129267

Shan Haoliang, Yu., & Zhouping. (2022). Strength, chloride ion penetration, and nanoscale characteristics of concrete prepared with nano-silica slurry pre-coated recycled aggregate. *Buildings*. https://doi.org/10.3390/buildings12101707

Shen, W., et al. (2018). Influence of manufactured sand's characteristics on its concrete performance. *Construction and Building Materials, 172*, 574–583.

Shi, L., et al. (2022). The effects of silanized rubber and nano-SiO$_2$ on microstructure and frost resistance characteristics of concrete using response surface methodology (RSM). *Construction and Building Materials*, *344*, 128226. https://doi.org/10.1016/j.conbuildmat.2022.128226

Shunbo, Z., et al. (2017). Experimental study on tensile strength development of concrete with manufactured sand. *Construction and Building Materials, 138*, 247–253.

Şimşek, O., Pourghadri Sefidehkhan, H., & Gökçe, H. S. (2022). Performance of fly ash-blended Portland cement concrete developed by using fine or coarse recycled concrete aggregate. *Construction and Building Materials*. https://doi.org/10.1016/j.conbuildmat.2022.129431

Song, Gao, et al. (2022). A comprehensive analysis of pore structures and performances of mineral admixtures modified recycled aggregate concrete based on experiment and theory. *Construction and Building Materials*. https://doi.org/10.1016/j.conbuildmat.2022.129451

Sun, X., Li, T., Shi, F., Liu, X., Zong, Y., Hou, B., et al. (2022). Sulphate corrosion mechanism of ultra-high-performance concrete (UHPC) prepared with seawater and sea sand. *Polymers*, *14*(5), 971. https://doi.org/10.3390/polym14050971

Tam Vivian, W. Y., Harshana, Wattage, Le Khoa, N., Anthony, Buteraa, & Mahfooz, Soomro. (2020). Methods to improve microstructural properties of recycled concrete aggregate: a critical review. *Construction and Building Materials*. https://doi.org/10.1016/j.conbuildmat.2020.121490

Tao, Li., Meng, Zhan, Chen Xiuyun, Xu., Fan, Wang Sheliang, & Xinxin, Liu. (2022). Study on carbonization characteristics and deterioration mechanism of recycled concrete with tailings and polypropylene fiber. *Polymers*. https://doi.org/10.3390/polym14142758

Vladimirovna, Aleksandrova Olga, Vinh, Quang Nguyen Duc., Igorevich, Bulgakov Boris, Viktorovich, Fedosov Sergey, Alekseevna, Lukyanova Nadezhda, & Borisovna, Petropavlovskaya Victoria. (2022). The effect of mineral admixtures and fine aggregates on the characteristics of high-strength fiber-reinforced concrete. *Materials*. https://doi.org/10.3390/ma15248851

Wisal, A. C. W. L. (2023). Evaluating fracture parameters of basalt fiber reinforced and pozzolana slurry modified recycled concrete produced from waste. *Structures*. https://doi.org/10.1016/j.istruc.2023.02.111

Wisal, A., & CW, L. (2023). Multicriteria performance assessment of sustainable recycled concrete produced via hybrid usage of basalt, polypropylene and glass fiber. *Construction and Building Materials*. https://doi.org/10.1016/j.conbuildmat.2023.132462

Xin, Wang, Yurong, Yan, Xiaofang, Tong, & Yongfan, Gong. (2022). Investigation of mineral admixtures on mechanical properties of alkali-activated recycled concrete powders cement. *Buildings*. https://doi.org/10.3390/buildings12081234

Xu, J., et al. (2022). Study on erosion characteristics and mechanisms of recycled concrete with tailings in salt spray environments. *Buildings, 12*(4), 446–446.

Xu, S., Gao, P., Huang, L., Tang, L., Gu, X., & Wang, L. (2022). Experimental research on mechanical and shrinkage properties of alkali activated low-carbon green concrete. *Materials*, *15*(17), 5984. https://doi.org/10.3390/ma15175984

Yang, Li., Qirui, Zhang, Ruijun, Wang, Xiaobin, Xiong, Yan, Li., & Jiayu, Wang. (2022). Experimental investigation on the dynamic mechanical properties and microstructure deterioration of steel fiber reinforced concrete subjected to freeze-thaw cycles. *Buildings*. https://doi.org/10.3390/buildings12122170

Yang, R., et al. (2019). The physical and chemical impact of manufactured sand as a partial replacement material in ultra-high performance concrete (UHPC). *Cement and Concrete Composites, 99*, 203–213.

Yanru, Z. H. A. O., Fangfang, L. I. U., & Lei, W. A. N. G. (2020). Modeling of the compressive strength of basalt fiber concrete based on pore structure under single-side freeze-thaw condition. *Materials Review, 34*(12), 12064–12069.

Ye, P., Chen, Z., & Su, W. (2022). Mechanical properties of fully recycled coarse aggregate concrete with polypropylene fiber. *Case Studies in Construction Materials*, *17*, e01352. https://doi.org/10.1016/j.cscm.2022.e01352

Yuanxun, Zheng, Jingbo, Zhuo, Yamin, Zhang, & Peng, Zhang. (2022). Mechanical properties and microstructure of nano-SiO2 and basalt-fiber-reinforced recycled aggregate concrete. *Nanotechnology Reviews*. https://doi.org/10.1515/ntrev-2022-0134

Publisher's Note

Xiong Wei   Lecturer (1984.11-) at the Department of Architecture and Engineering, Wuhan City Polytechnic, Research Direction: Building Materials.

Wang Xiaoqing   Associate Professor (1974.09-) at the Department of Architecture and Engineering, Wuhan City Polytechnic, Research Direction: Engineering Management, Building Materials.

Li Chunmei   Lecturer (1983.02-) at the Department of Architecture and Engineering, Wuhan City Polytechnic, Research Direction: Engineering Management.